Serial Compression Effects on Porosity, Diffusion, Permeability, and Water Droplet Contact Angle of the Gas Diffusion Layer in Polymer Electrolyte Membrane Fuel Cells

by

James Park

A thesis
presented to the University of Waterloo
in fulfillment of the
thesis requirement for the degree of
Master of Applied Science
in
Mechanical and Mechatronics Engineering

Waterloo, Ontario, Canada, 2020

Author's Declaration

I hereby declare that I am the sole author of this thesis. This is a true copy of the thesis, including any required final revisions, as accepted by my examiners.

I understand that my thesis may be made electronically available to the public.

Abstract

The polymer electrolyte membrane (PEM) fuel cell is an electrochemical device that directly converts the chemical energy of hydrogen and oxygen into electricity with water and heat as byproducts. It is very promising to wean or supplant our dependence on fossil fuels for energy. However, improvements to the cost, performance, and durability are remaining challenges before this green technology can be fully adopted. Increasing the current density in an operating fuel cell will degrade the cell potential, and both are required for high performance. The losses occurring at this level of performance is referred to concentration overpotential and is a result of inefficiencies in the reactant, primarily oxygen, transport through the gas diffusion layer (GDL) to the electrochemical sites, which may also be blocked by excess water. The GDL is typically made of a random arrangement of carbon fibers with total thickness under 400 μm. No two samples are truly identical. A better understanding of the parameters that can predict the gas transport and the water removal will help to further optimize the PEM fuel cell to achieve its performance goals for commercialization.

Within an operating fuel cell, there is an inhomogeneous distribution of the stresses. The stresses alter the structure of the GDL and, in turn, affect the reactant transport and water droplet behaviour. By investigating the changes of the same sample over multiple compressions, three aspects are studied in the present thesis research: (i) gradual changes in the pore structure while maintaining other sample properties constant, (ii) the effect of these pore structure changes on gas transport phenomena in the GDL, and (iii) the effect of these changes on water droplet behaviour on the surface of the GDL. Many factors are involved in these two phenomena, but, in the case of the gas transport, are typically characterized by the normalized pore volume, or porosity, of the sample. This generalization of the other parameters into porosity limits the circumstances in which the model can be applied. Additionally, by using the same sample across multiple different tests, comparisons can be directly observed between them. Currently, there is a lack of experimental data that connects all of these phenomena.

In the present thesis research, the GDL pore structure is manipulated by undergoing compression in a hydraulic press. Upon unloading of the stress, a permanent change in thickness is observed. The normalized change in thickness, inspired from the material sciences, is referred to as “residual strain”. Applying the concept of serial

testing, each sample, once compressed, undergoes a battery of tests to extract information about the phenomena. Once completed, the same sample is compressed further and the process repeats. The GDL pore structure is experimentally characterized by the method of standard porosimetry (MSP), which operates on the principle of capillary equilibrium. MSP reveals the porosity, pore size distribution (PSD), pore surface area, and the mean pore radius. The permeability constant is measured using Darcy's law via a modified Loschmidt Cell, while the effective diffusion coefficient is measured using Fick's second law of diffusion via a Loschmidt Cell. Additionally, the water droplet behaviour is characterized via the Cassie-Baxter model on a goniometer. Assumptions are validated throughout the experiments. With the detailed pore structure available, new correlations and patterns are observed which show strong linearity between multiple samples. This is in contrast to the non-linear empirical models.

The experimental studies presented in the present thesis is of great significance to (i) understand how the pore structure changes in response to compression, (ii) understand how these pore structure changes relate to reactant gas transport phenomena, such as the effective diffusion coefficient and permeability, and (iii) understand how the surface properties may not be similar to the bulk properties and how those differences and similarities can be used to predict water droplet behaviour, and, thus, be used to better predict performance in PEM fuel cells.

Acknowledgements

I would like to express my gratitude to my supervisor Dr. Xianguo Li for his guidance, support, and encouragement throughout my MASc degree. I would like to also thank my committee members for taking their time to review my thesis and for providing constructive comments. Their comments are highly appreciated.

A sincere thanks to Dr. Jian Zhao for giving me the inspiration of the seedling idea that would eventually grow into my thesis in its current form and the numerous discussions on the experimental methods. Further, I would like to thank Dr. Samaneh Shahgaldi and Dr. Ibrahim Alaefour for making themselves available to discuss issues in the interpretations of my results.

Furthermore, I would like to express my gratitude to the technical support staff who would come to my rescue if any of the lab apparatus failed. Lastly, I would like to express my eternal gratitude to my fiancée, Marie, whose support and patience helped me get through the last leg of this journey amidst the COVID-19 pandemic.

Table of Contents

List of Figures

List of Tables

List of Abbreviations

AFC	Alkaline Fuel Cell
BET	Brunauer-Emmett-Teller
CL	catalyst layer
CT	computed tomography
FEP	fluorinated ethylene propylene
GDL	gas diffusion layer
MCFC	Molten Carbonate Fuel Cell
MEA	Membrane Electrode Assembly
MIP	Mercury Intrusion Porosimetry
MP	mega-pixel
MPL	micro-porous layer
MSP	Method of Standard Porosimetry
PAFC	Phosphoric Acid Fuel Cell
PDMS	polydimethylsiloxane
PEM	Polymer Electrolyte Membrane
PSD	pore size distribution
PTFE	polytetrafluoroethylene
Re	Reynolds number
RSS	root-sum-square
SCCM	standard cubic centimetre per minute
SEM	scanning electron microscope
SOFC	Solid Oxide Fuel Cell
TGA	thermogravimetric analysis

List of Symbols

A	area
C	concentration
$\mathcal{D}$	diffusion coefficient
f	fraction
J	molar mass flux
k	permeability constant
k_b	Boltzmann's constant
K_c	Kozeny constant
m	mass
M	molar mass
$\dot{m}$	mass flux
p	pressure
P	Perimeter
R	resistance
R_{igl}	ideal gas constant
r	carbon fiber radius
$\bar{r}$	mean radius
r_{pore}	pore radius
S	surface area
$\mathcal{s}$	residual strain
T	temperature
t	time
V	volume
$\vec{v}$	superficial velocity
x	x-dimension

Greek letter

β	coefficient of inertia
γ	surface energy
ε	porosity

θ	contact angle
μ	fluid viscosity
ρ	density
σ	surface tension
τ	tortuosity

Subscripts and Superscripts

air	air
app	apparent or observed
b, i	bulk, species i
b,0	bulk, 0% PTFE
bulk	bulk (material)
cap	capillary
CF	carbon fiber
dry	dry
eff	effective
eq	equivalent
hyd	hydraulic
i	species 'i'
ij	bulk (diffusion)
in	in
l-s	liquid-solid
max	maximum
out	out
pore	pore
sat	saturated
s-g	solid-gas
s-l	solid-liquid
solvent	solvent

Chapter 1

Introduction

1.1 Background

In an era of fossil fuel combustion and increasing levels of carbon dioxide into our atmosphere, new technologies are emerging to meet a growing population's energy needs while maintaining an environmental and social conscience. Electric vehicles powered by batteries have since become mainstream in the personal vehicle market in developed nations. For shorter travel distances, given the relatively long time that is required to recharge the batteries, this is an effective means to address climate concerns and maintain a lifestyle that many have grown accustomed. However, in the commercial transportation industry, where the run-time of a vehicle, like a bus or a train, is measured in hours instead of minutes, the implementation of battery-operated electric vehicles is difficult [1-2]. An alternative is the hydrogen fuel cell, an electrochemical device with similarities to a battery except one that you can refuel quickly (in minutes) instead of re-charge over a prolonged time (in many hours).

The fuel cell takes the chemical energy of the fuel and oxidant and converts it directly into usable electrical energy [3]. While fundamentals of the fuel cell remain constant, different types of fuel cell technology have been developed, differing in their electrolyte and fuel type. The primary types are: polymer electrolyte membrane (PEM) fuel cells, alkaline fuel cells (AFCs), molten carbonate fuel cells (MCFCs), solid oxide fuel cells (SOFCs), and phosphoric acid fuel cells (PAFCs) [3]. The PEM fuel cell is the

most promising type in the transportation industry for its relatively low operating temperatures, high energy-conversion efficiency, rapid start-up capability, quiet operation, and near-zero emissions [1].

However, the commercialization of PEM fuel cells is currently hindered by the high costs, long term durability, and the performance [4]. These challenges are the main motivations for this research.

1.2 PEM Fuel Cell Components and Working Principles

The principle components of a PEM fuel cell unit consist of a symmetrical design around a solid membrane flanked by an electrode, flow channel, and distribution plate as shown in **Fig. 1-1**. Each electrode is supported by a gas diffusion layer (GDL) and a catalyst layer (CL), where the electrochemical reactions occur. At the anode, hydrogen gas is supplied to the flow channels and then distributed through the GDL to the CL. At the anodic CL, the hydrogen gas (H_2) molecules are oxidized into protons (or hydrogen ions) and electrons. The protons are then transported through the PEM towards the cathodic CL while the electrons are forced back through the anode solid material towards the distribution plate into an external electrical circuit towards the cathode. Concurrently, oxygen gas (O_2) is supplied to the cathodic CL in an identical fashion. At the cathodic CL, the oxygen molecules react with the transported anodic protons and electrons to produce water (H_2O), an electric current in the external circuit, and heat.

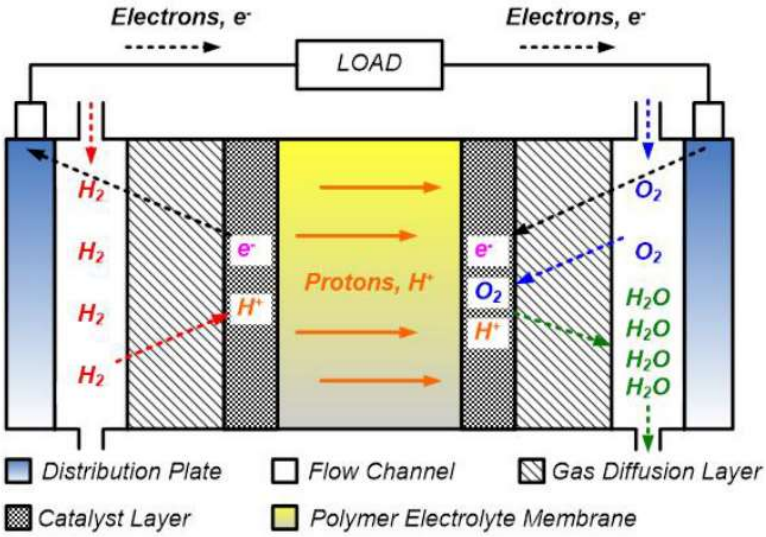

Fig. 1-1. Schematic representation of a PEM fuel cell unit with principle components identified [5].

The electrochemical reactions occurring at each electrode are referred to half-cell reactions. The hydrogen oxidation reaction occurs at the anode and is shown as:

$$H_2 \rightarrow 2H^+ + 2e^-$$

Meanwhile, at the cathode, the oxygen reduction reaction occurs and is shown as:

$$\frac{1}{2}O_2 + 2H^+ + 2e^- \rightarrow H_2O$$

By combining these two half-cell reactions, the overall chemical reaction in a PEM fuel cell is:

$$H_2 + \frac{1}{2}O_2 \rightarrow H_2O + \text{Electrcity} + \text{Heat}$$

The electrons that flow from the anode to the cathode, measured as electrical current, are conserved in the overall reaction.

1.3 PEM Fuel Cell Performance

In an operating PEM fuel cell, the actual cell potential is the electrical potential difference between the higher cathodic potential and the lower anodic potential [3]. When operating in ideal thermodynamically reversible conditions and pure reactants are supplied to the respective electrodes, the theoretical cell potential, also known as the reversible cell potential, is 1.22 V at standard conditions (25 °C and 1 atm) [3]. However, under actual operating conditions, continuous electrochemical reactions and their respective irreversibilities, the PEM fuel cell energy losses reflected as electric potential losses, or "overpotential". The overpotential results in a noticeable reduction in the cell potential down to 0.70 V for most cases [3].

As more current is drawn from the fuel cell, the cell potential gradually decreases. This phenomenon is best understood from a typical polarization curve, **Fig. 1-2**. This curve can be categorized into three different regions as identified by the significant source of overpotential: activation overpotential, ohmic overpotential, and concentration overpotential [3]. The activation overpotential represents the losses that are incurred from the initialization of the electrochemical reactions. The ohmic overpotential represents the losses that are associated with the proton transport through the solid membrane and the resistance of the electron transport from the anodic to cathodic CL. The concentration overpotential represents the losses incurred from insufficient mass transport to the CL. While these regions are identified by the main contributor of the losses, all of the sources of losses are concurrently occurring to different extents [6].

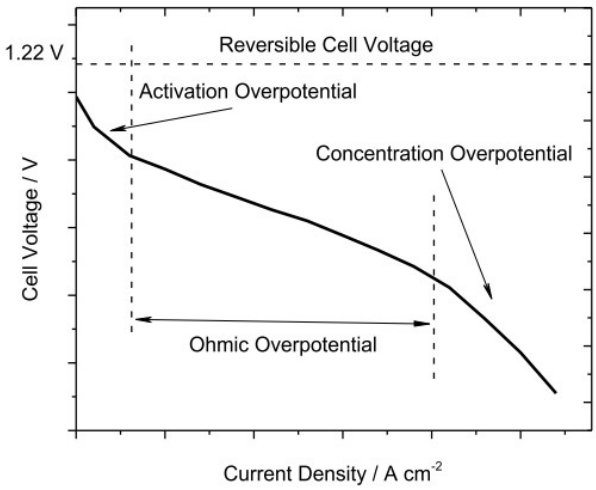

Fig. 1-2. A typical polarization curve for a PEM fuel cell [3].

To achieve practical power requirements and pressurize the system, multiple fuel cell units would be assembled together into a fuel cell stack [3-7]. A schematic of a fuel cell stack is shown in **Fig. 1-3**. By tightening the bolts, the end plates apply a load to the fuel cell units. The bipolar plates, which act as the flow distribution plate, then make better contact with the GDL of the electrodes also for the collection and transport of electric current. Due to the relatively low Young's modulus of the GDL in comparison to the bipolar plate, this causes a deformation to the GDL [8, 9]. The benefit of this added stress is that there will be a reduction of the interfacial contact resistance between the GDL and the bipolar plate, which is a constituent contributing to the ohmic overpotential [10, 11]. However, this will come at the expense of the gas transporting porous space in the GDL, further contributing to concentration overpotential. A delicate balance between reducing ohmic overpotential and increasing concentration overpotential exists in the optimal operations of a fuel cell stack [12-15].

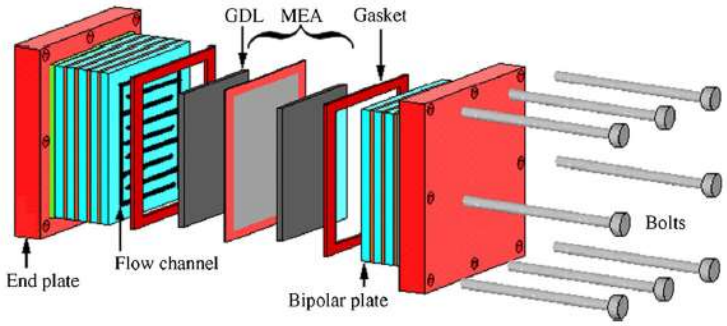

Fig. 1-3. A schematic of several PEM fuel cell units assembled into a fuel cell stack. MEA = membrane electrode assembly consisting of the membrane and two electrodes [7].

The mass transport of the reactants through the supporting GDL is critical in the effective operations of the PEM fuel cell. In addition to supplying the CL with the necessary reactants, the water produced at the cathode, particularly at high current densities, must be properly managed otherwise it will interfere with the reactant transport. The excess accumulation of water in the electrode is called “flooding” and negatively impacts PEM fuel cell performance [16-17]. Water removal occurs by transporting the water towards the pressurized flow channels where they can be removed from the system. Therefore, any studies into the reactant transport through the GDL should include an investigation into the water management of the system [18]. Addressing the mass transport limitations at high current densities is necessary to make PEM fuel cells smaller, lighter, and more cost-effective for commercial applications [3].

1.4 Features of the Gas Diffusion Layer

The GDL performs crucial roles in fuel cell operations by: (i) controlling the reactants and products to and from the CLs via the voids, (ii) providing electron and heat conduction through the solid core, and (iii) providing mechanical support to the relatively fragile CL. Ideally, the GDL should [4, 19-25]:

- provide a robust mechanical support to protect the membrane and CL from damage during assembly and long-term operations;
- have high reactant and product permeability to ensure an adequate supply of the reactants, especially oxygen, so that performance is limited to electrode kinetics while also removing generated water that transports in the direction opposite to the desired gas flow;
- be lightweight and thin to maximize the power-to-weight ratio to meet practical needs of commercialization;
- have high electrical conductivity to minimize the ohmic overpotential by effectively transporting the electrons between the anodic CL to the distribution plates and then back to the cathodic CL; and
- have high thermal conductivity to effectively remove the heat from the MEA where it is produced.

Up to now, a carbon fiber-based material is used to meet these requirements. These materials are commercially available from various brands, like Toray. To enhance the mechanical robustness of a carbon fiber paper material, a binder is used to maintain the cohesion of the material [19]. As seen in **Fig. 1-4**, this material is mostly void space that would allow for maximal mass transport through it. To enhance the water management, polytetrafluoroethylene (PTFE), known for its ability to repel water, is often added to improve the performance of the material. Other hydrophobic agents can be used, such as fluorinated ethylene propylene (FEP) [26] and polydimethylsiloxane (PDMS) [27]. The use of binder and the application of PTFE differs between the brands and are not publicly available. The mass production of these materials, combined with the naturally disordered arrangement of the carbon fibers, can cause inhomogeneity across the same sample [19, 28, 29].

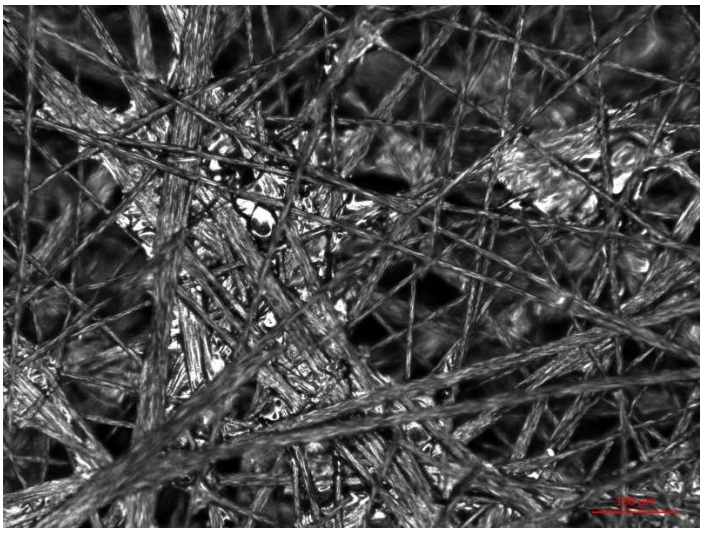

Fig. 1-4. A sample image of an untreated Toray TGP-H-120 GDL at 260X magnification by optical microscope. Individual fibers and binder can be seen.

1.5 Gas Transport through the Gas Diffusion Layer

The gas transport through the GDL is accomplished through diffusive and convective transport mechanisms. The gas transport is a function of pore radii, tortuosity, and porosity [30]. Tortuosity is the ratio of the actual flow path to the straight line path and can vary between 1.6 – 2.0 in the typical GDL sample [31]. Porosity is the pore (or void)

volume to the total volume. Empirical models typically correlate only porosity to the respective transport model, while ignoring the other two parameters.

1.5.1 Diffusion

Diffusion is the net motion of molecules from one location to another as a result of random molecular motion [19, 31, 32]. While the diffusion process can be driven by multiple methods, the diffusion is popularly associated with motion down a concentration gradient. The bulk diffusion coefficient, $\mathcal{D}_{ij}$, is the measure of the diffusion between two species, i and j, driven solely by the intermolecular collisions without any interference from the environment. Fick (1855) was the first to develop a formulation of the diffusion of mass by recognizing that heat conduction, as derived by Fourier (1822), followed a similar process [32]. Fick had assumed that the diffusive mass flux is proportional to the concentration gradient:

$$J = -\mathcal{D}\frac{\partial C}{\partial x} \tag{1-1}$$

where J is the molar mass flux in $mol \cdot m^{-2} \cdot s^{-1}$, C is the concentration of the gas species in $mol \cdot m^{-3}$, x is the space coordinate in m, and $\mathcal{D}$ is the diffusion coefficient in $m^2 \cdot s^{-1}$.

1.5.2 Convective Mass Transport

The other method of reactant gas transport through the GDL is by convection. Convective mass transport, or gas permeability, is the mass transport down a pressure gradient. This relationship can be determined by the Darcy-Forchheimer Equation [33]:

$$-\nabla p = \frac{\mu}{k}\vec{v} + \beta\rho|\vec{v}| \cdot \vec{v} \tag{1-2}$$

where p is the pressure in Pa, μ is the fluid viscosity in Pa·s, k is the permeability coefficient in m^2, $\vec{v}$ is the superficial velocity in $m \cdot s^{-1}$, β is the coefficient of inertial flow resistance in m^3, and ρ is the gas density in $kg \cdot m^{-3}$. The second term in this formulation is referred to as the inertial term and is only relevant at high velocities where the Reynold's number (Re) is greater than 1.

1.6 Water Management

In an effort to maximize PEM fuel cell performance, multiple water management strategies are employed. Water management is a major influence on the oxygen reduction

reaction. In the fuel cell operation, water is produced at the cathodic CL as a by-product of the oxygen reduction reaction. Additionally, some water can also be transported through the membrane in both directions: towards the anode if sufficient hydraulic pressure is built up at the cathodic CL resulting in a phenomenon called "back diffusion" [19] and towards the cathode as protons are transported through the membrane called "electroosmosis". These phenomena are schematically shown in **Fig. 1-5**. One of the strategies employed is the application of a microporous layer (MPL) between the GDL and the CL. The pore sizes are significantly smaller in the MPL in comparison to the GDL and serve as a passive pressure valve to retain optimal moisture levels at the CL [34]. As mentioned earlier, the GDL can also be treated with a hydrophobic agent, like PTFE, to assist the transmission of water through the GDL towards the flow channels. The addition of the hydrophobic agent can markedly alter the microstructure of the GDL as shown in **Fig. 1-6** in comparison to **Fig. 1-4**. The addition of the hydrophobic agent shows a tendency to increase the carbon fiber diameter in addition to occupying some of the void spaces necessary for mass transport.

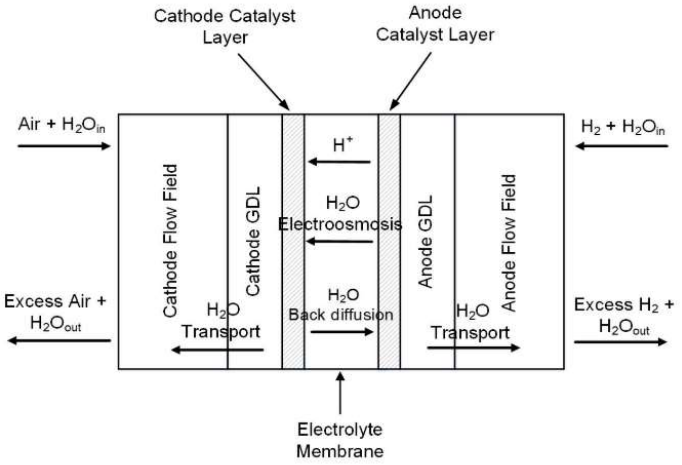

Fig. 1-5. Schematic of water transport in the PEM fuel cell [35].

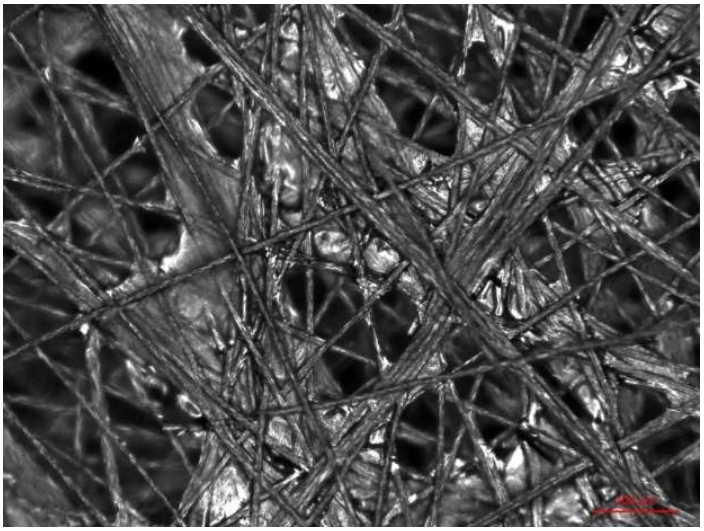

Fig. 1-6. Optical microscopy image of a Toray TGP-H-120 sample treated with 60% PTFE (mass/mass).

As the water migrates towards the surface of the GDL inside of the flow channels, water droplets begin to form. This is schematically shown in **Fig. 1-7**. Once in the flow channels, the water can be removed from the system by the reactant pressure flow [36]. Sometimes, however, the droplet may not properly detach from the surface, called "pinning" and continue to grow until it occludes the flow channel [17, 37]. This phenomenon is called "plugging". The detachment of the water droplet, and its subsequent removal from the system, is correlated to the water droplet contact angle.

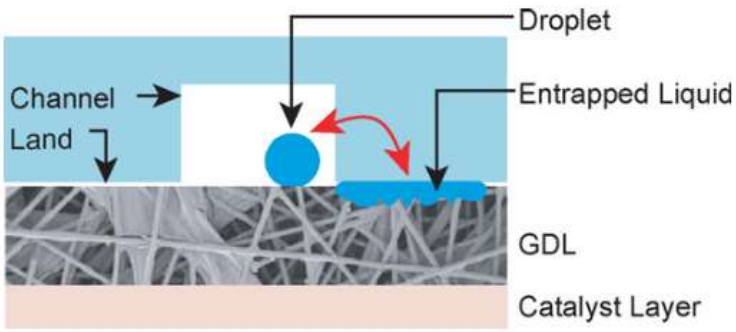

Fig. 1-7. Schematic of the formation of water droplets and other accumulations towards the surface of the GDL [38].

As a water droplet forms atop a rough surface of the GDL, the droplet creates an angle with the surface at the interface of the edge of the water droplet. This observed,

also known as apparent, contact angle, θ_{app}, is created from the interaction between the surface energies (γ) between solid-gas (s-g), solid-liquid (s-l), and liquid-gas (l-g) interfaces. This relationship is commonly represented by Young's equation [39]:

$$\cos\theta_{app} = \frac{\gamma_{s-g} - \gamma_{s-l}}{\gamma_{l-g}} \tag{1-3}$$

However, this equation assumes that the surface is perfectly flat and homogeneous, which the GDL surface is not. To correct for the surface roughness, a roughness factor (f_r) can be introduced as a ratio of the real (rough) surface to the geometric (flat) surface [39]. This relationship implies that the roughness factor is always greater than unity. Due to the cosine relationship, 90° is often the threshold between the categories [27, 40]: hydrophilic and hydrophobic. This analytical interpretation of hydrophilicity/hydrophobicity, which is supposed to help characterize the behaviour of water droplets on a surface, does not always hold true [20]. This implies that the roughness factor induces a surface more strongly on the same side of its hydrophilicity or hydrophobicity.

A schematic differentiating between a hydrophobic surface and a hydrophilic surface is found in **Fig. 1-8**. The desired property of the GDL surface is for greater hydrophobicity. A hydrophobic surface is associated with easier detachment of a water droplet [37]. While many attempts at producing new materials with improved hydrophobic properties have been made, the highest contact angle of any pure and smooth surface is approximately 130° [27]. It was observed that, on the lotus leaf, water droplet contact angles can exceed this material limitation [27]. Consistent with the concept of the roughness factor, it is the geometry of the surface that contributes a large portion to the observed contact angle.

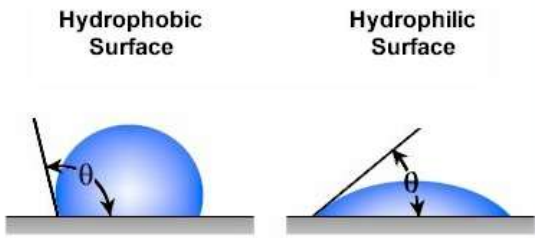

Fig. 1-8. Schematic of the differences in contact angle with respect to the categories of hydrophobic and hydrophilic (adapted from [41]).

In an attempt to capture the roughness and inhomogeneity of a real surface, Cassie and Baxter [42] proposed a system of equations to predict the apparent contact angle:

$$\begin{cases} \cos\theta_{\text{app}} = \sum f_i \cos\theta_i \\ \sum f_i = 1 \end{cases} \tag{1-4}$$

where f_i is the fraction of the water droplet interacting with species i and θ_i is the reference contact angle of species i to water. A modification to this model is the Wenzel equation, which is identical to the Cassie-Baxter equation except, since it is assumed that the water droplet does not interact with air that f_{air} is equal to zero. The two models are depicted in **Fig. 1-9**. These models do not need to account for the surface roughness [27].

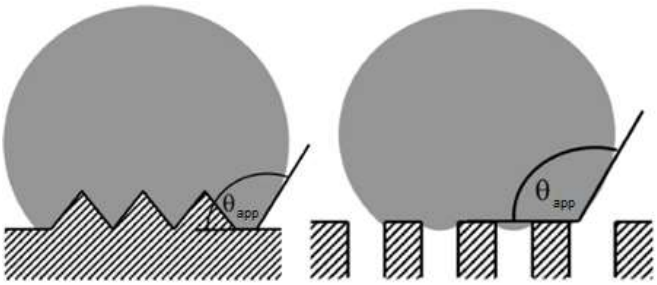

Fig. 1-9. Schematic showing the pure Wenzel condition (*left*) and the pure Cassie-Baxter condition (*right*).

1.7 Objectives and Scope of the Thesis

Extensive effort has been made to achieve a high-performance PEM fuel cell to reach mass commercialization. To investigate optimal design parameters, many studies have been conducted to properly characterize the relationship of the GDL microstructure to gas transport and contact angle, though seldom at the same time. These empirical models are often correlated to the porosity. Accurate characterization is necessary to predict the mass transport limitations for high current density operations. Unfortunately, all of the data is based on multiple samples with varying properties owed to the disordered nature of commercially available GDL samples. All of the other parameters for transport and water droplet formation end up being merged into the porosity.

Therefore, the objectives of this thesis study are: (i) to isolate changes in porosity and pore radii while maintaining the other parameters, (ii) to investigate how these direct

changes in the pore structure relate to diffusion and permeability, and (iii) to investigate how these pore structure changes alter the water droplet contact angle.

In order to isolate only changes to porosity and pore radii, while controlling the other parameters, serial testing is employed. This differs from traditional *ex-situ* fuel cell experiments in which different samples are used for each collected datum point. In the context of this research, it involves compressing a sample and running a battery of tests to collect the requisite data, followed by another compression. The principle working assumption is that by using the same sample, the other material properties and sample-to-sample variations do not exist. By investigating the changes of the material properties in between a series of compressions, the only parameters that have changed are the porosity and pore radii.

This thesis is comprised of five chapters. In chapter one, the importance of mass transport and water management as it pertains to the GDL are described. In chapter two, a literature review of experimental and numerical studies investigating our understanding on the mechanisms behind the mass transport and water droplet formation are explored. In chapter three, a detailed discussion of the *ex-situ* experimental techniques that have been developed to estimate these parameters is provided. Many of the assumptions used through-out these experiments are also validated. In chapter four, the results of the experimental investigations are presented and new preliminary correlations are revealed. Lastly, chapter five presents a summary of the main conclusions derived from the investigations into serially compressed GDL samples and provides recommendations for future studies.

Chapter 2

Literature Review

In this chapter, a comprehensive literature review is conducted with a focus on the effect on: (i) the compression of the GDL, (ii) the pore structure, (iii) gas transport, (iv) water droplet formation on the surface, and (v) the assumptions employed in these investigations. Most techniques employed in *ex-situ* experiments are effectively destructive [24] to the sample, and this is undesirable in this study.

2.1 Compression of the GDL

Investigations into the effect of compressive stresses, a form of degradation [11], can provide necessary insight to address the long term durability of the fuel cell.

2.1.1 *In-Situ* Compression

Studies conducted at the fuel cell unit- or stack- level are included in this section. In an operating fuel cell stack, the end plates are bolted into place in order to pressurize the system to prevent gas leaks and ensure good contact between the bipolar plates and the electrodes. Many of these studies were conducted to minimize the interfacial contact resistance between these two components, thereby reducing the total ohmic losses [10, 42].

In the process of minimizing the ohmic overpotential, there is eventually a detrimental decrease in performance of the fuel cell. Optimization studies report a wide

range at which the fuel cell should be clamped to achieve the best balance between decreasing ohmic overpotential and decreasing the available mass transport through the electrode: 0.5 – 1.0 MPa [15, 42], 1.0 – 2.0 MPa [13], and 1.5 – 3.0 MPa [14]. Numerical studies have shown that the compressed GDLs play a significant role in the performance, particularly when multiple phases are properly considered [44].

The main advantage of conducting *in-situ* experiments is that the changes in the variables can be directly correlated to performance. However, due to the complexity of the system, it is difficult to isolate the root cause. To overcome the complexity, particularly for numerical explorations, assumptions are employed to improve the convergence of the solutions. Depending on the validity of such assumptions, it could be a matter of adjusting the input parameters to match that of the comparable experimental studies used for validation.

2.1.2 *Ex-Situ* Compression

Ex-situ studies allow for the isolation of the investigation of specific phenomena and allow for greater control of the remaining variables. Studies involving the direct manipulation of the GDL in isolation of the electrochemical kinetics of the operating fuel cell are investigated in this section.

Studies on the *ex-situ* compression on the GDL typically come in two varieties: focus on the macrostructure or focus on the microstructure. Changes in thickness of the GDL are one type of study. It has been reported that the presence of a hydrophobic agent aids in the resistance to thickness change [45]. Additionally, the GDL will undergo both elastic and plastic deformation when a stress is applied [46], as shown in **Fig. 2-1**. Resistance to deformation is an important characteristic when trying to minimize the interfacial contact resistance of the GDL to the bipolar plate [7, 9, 46]. Finite element analyses and statistical analysis of variance have shown that higher through-plane stiffness will yield better contact [48]. Other investigations into the stress distribution found in the fuel cell units of a fuel stack experience a non-uniform stress distribution [48-50]. This non-uniformity may help to explain the discrepancy between the optimal clamping stress of the fuel cell [52]. Changes with a focus on the microstructure are covered in the following section as they are often coupled with imaging techniques.

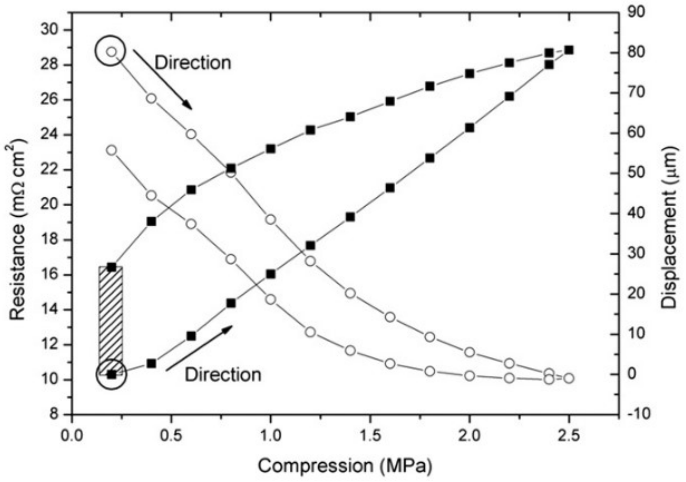

Fig. 2-1. Relationship between the *in-situ* strain (during loading) and the residual strain (unloaded thickness) of a TGP-H-120 sample. Effect on contact resistance also shown [46].

The effect of compression on gas transport and water droplet contact angle can be found in **Sections 2.3** and **2.4**, respectively.

2.2 Pore Structure

Studies have been undertaken to investigate the pore structure. Imaging techniques are used for the direct observation of the pore structure. Alternatively, the bulk property of porosity, the normalized volume of the pore space to the total (bulk) volume of a given sample, can provide useful information in understanding the pore structure. Another important parameter to evaluate the pore structure is the PSD. A detailed explanation of the PSD is available in **Section 3.4.1**.

2.2.1 Imaging Techniques

Direct visualization of the GDL sample can lead to greater understanding into the interactions with gas and liquid.

A scanning electron microscope (SEM) is a popular tool to visualize the GDL and nanoscale components like the MPL and CL [19, 26, 52]. While it provides high magnification, it requires software and image analysis algorithms to extract pore structure [54].

Another imaging technique used is X-Ray micro-computed tomography (CT). This technique is often coupled with numerical studies as it is able to penetrate into the sample and a three-dimensional model can be made to match that of the sample [54-57].

The resolution is particularly limited in comparison to the SEM with the best micro-CTs able to resolve down to 1.3 μm [59]. Additionally, due to similar X-ray absorption of the carbon fibers and hydrophobic agents, it is unable to discern between the two materials [55].

Another option for direct visualization of a carbon paper sample is optical microscope. Despite being readily available and relatively affordable in comparison with other imaging methods, this technique is poorly represented in literature. The optical magnification has a resolution that is limited only to the camera used to obtain images. It is possible to resolve 1 μm length scales at 260X magnification. For these reasons, this method is used in this study.

2.2.2 Porosity Measurements

Direct porosity measurements are relatively simple to obtain. The typical method is through a process of liquid intrusion. By knowing the bulk volume of a given sample, the porosity can be computed from the volume of the working liquid that occupies the pore space of the sample, calculated from the increased mass of the, now, saturated sample and the density of the working liquid. Water can be used as the working liquid to identify the hydrophilic porosity, the water conducting pore space. It is generally accepted that small pores and the presence of a hydrophobic agent that not all pores are suitable for the transmission of water [60]. The hydrophilic porosity should be less or equal to the bulk porosity, which could be obtained by using a wetting fluid, like octane.

2.2.3 Pore Size Distribution

Two of the most traditional methods of investigating the PSD are mercury intrusion porosimetry (MIP) [61] and gas adsorption. Mercury is a fully wetting fluid with a contact angle on all surfaces of 0°. As it is a pure element, it is capable of penetrating pores down to the atomic level. However, because of the density of mercury, high pressures are often required for the mercury to fully penetrate the sample causing deformation to the pore structure. Additionally, from a practical perspective, even if the sample remains intact, the use of mercury effectively destroys the sample due to its toxicity despite being reported to be non-destructive [24]. The results from Radhakrishnan and Haridoss, who conducted MIP in between compressions in series, show a non-converging trend in the compressed samples [62]. This trend is contrary to

the other reported trends of successive compression [45], suggesting that MIP is a destructive test to the sample. In contrast, the gas adsorption technique typically uses nitrogen gas and computes the surface area by the amount of gas that is adsorbed onto the pore surface using the Brunauer-Emmett-Teller (BET) method. It is excellent at resolving very small pores in the sub-nm range but is not suitable for dealing with a wide range of pore sizes, as found in the GDL [31]. The imaging techniques, like SEM and X-ray micro-CT can be used to determine PSD but rely on data-processing algorithms.

Another technique is the Method of Standard Porosimetry (MSP). It is capable of detecting a broad range of pores (0.3 nm to 300 μm) without damaging the sample [31]. More information on the working principles of this method is available in **Section 3.4.1**. For this reason, this method is used in this study.

2.2.4 Summary

When investigating the effects of compression on the GDL with relatively large pores in comparison to the MPL and CL, numerous techniques are available for assessing the pore structure. A summary of some of the representative research conducted is available in **Table 2-1.** Studies relating pore structure to gas transport or water droplet contact angle are excluded from this summary.

Table 2-1. Summary of pore structure investigations of GDL paper.

Sample	PTFE (w/w)	Comp. (S/P)	Porosity		Pore Size Distribution	Source
			Meas.	Calc.		
GDL 30BA	5%	S	-	X	X-ray micro-CT	[58]
TGP-H-120	5% - 20%	S	-	X	X-ray micro-CT	[56]
SGL	5%, 20%	P	X	-	MSP	[63]
TGP-H-120	0% - 60%	S	X	-	MSP	*THIS STUDY*

NOTE: PTFE = polytetrafluoroethylene treatment; Comp. (S/P) = Compression (Serial/Parallel); Meas./Calc. = Measured/Calculated Porosity; X = employed method

2.3 Gas Transport

Numerous studies, experimental and numerical, have been conducted in the study of gas transport through the GDL. *In-situ* experiments are unable to distinguish the impact of either diffusion or convective mass transport, though these occur simultaneously [64]. Only *ex-situ* experiments will be able to separate the two types of gas transport to the

electrochemical sites. Numerical studies have difficulty managing both of these transport mechanisms because they operate with different slip boundary conditions [65].

2.3.1 *In-Situ* Experiments

Gas transport to the CL cannot be directly measured in an active fuel cell. Since the cell voltage is an interaction of the activation overpotential, ohmic overpotential, and concentration overpotential, if the first two overpotentials are very well characterized, the gas transport to the reaction sites can be correlated to the concentration overpotential [66]. In contrast, numerical studies of *in-situ* fuel cells often assume a macro-homogeneous continuum approximation such that the porous medium is homogeneous [54, 66].

2.3.2 Gas Diffusion

The principles of gas diffusion were discussed in **Section 1.5.1**. In this thesis research, diffusion down a concentration gradient is of interest.

2.3.2.1 Experimental Methods

While there are several experimental methods to determine the diffusion coefficient, each has their disadvantages, like long test times, greater uncertainty, and difficulty controlling the parameters. The best and most widely used method is the closed-tube method or Loschmidt Cell [67-69]. For its high accuracy, relatively short experimental time, and simple configuration, the closed tube method via a Loschmidt Cell is used to determine the diffusion coefficients in this study.

2.3.2.2 Empirical Models

Diffusion in pores is driven by three mechanisms: bulk diffusion, Knudsen diffusion, and surface diffusion [70]. Surface diffusion, as the name implies, only occurs at or near the pore surfaces, however the GDL pore sizes are relatively large and this effect could be neglected. On the other end of the spectrum is bulk diffusion, driven solely by intermolecular collisions. Meanwhile, Knudsen diffusion is in-between interacting with all. The Knudsen number, K_n, correlates which regime the flow is in and defined by:

$$K_n = \frac{\lambda}{l} \tag{2-1}$$

where λ is the mean free path of the gas molecules and l is the characteristic length scale of the porous medium (e.g. pore diameter). By assuming ideal gas properties, the mean free path can be calculated:

$$\lambda = \frac{k_B T}{4\sqrt{2} p \pi r_{\text{pore}}^2} \tag{2-2}$$

where k_B is the Boltzmann constant, p is the pressure, and r_{pore} is the pore radius. When $K_n < 0.1$, bulk diffusion dominates but when $K_n > 10$, Knudsen diffusion dominates. The mean free path of oxygen gas at 25 °C and 1 atm is approximately 70 nm [69] and since the pore sizes are greater than 1 μm in the GDL, bulk diffusion dominates.

In the presence of a porous medium, the effective diffusion coefficient, $\mathcal{D}_{\text{eff}}$, of the porous sample can be described as a function of the sample such that:

$$\mathcal{D}_{\text{eff}} = \frac{\varepsilon}{\tau} \mathcal{D}_{ij} \tag{2-3}$$

where τ is the tortuosity of the porous sample, and $\mathcal{D}_{ij}$ is the bulk diffusion coefficient of the binary gases. The bulk diffusion coefficient of the oxygen and nitrogen binary gas mixture can be calculated with Marrero and Mason's model [71]:

$$\ln\left(p \cdot \mathcal{D}_{ij}\right) = \ln(1.13 \times 10^{-5}) + 1.724 \ln T \tag{2-3}$$

where p is the pressure in atm, $\mathcal{D}_{ij}$ is the bulk diffusion coefficient in $cm^2 \cdot s^{-1}$, and T is the temperature in K. This model is widely used because the uncertainty is about 3% [71].

Many empirical models end up using only porosity as the parameter for diffusion, as summarized in **Table 2-2**.

Table 2-2. Empirical models for predicting the effective diffusion coefficient of a sample.

Model	Effective Diffusion Coefficient	Note	Source	Eq. #
Bruggeman	$\mathcal{D}_{\text{eff}} = \varepsilon^{1.5} \mathcal{D}_{ij}$	spherical particles	[72]	(2-4)
Neale & Nader	$\mathcal{D}_{\text{eff}} = \frac{2\varepsilon}{3-\varepsilon} \mathcal{D}_{ij}$	spherical particles	[73]	(2-5)
Tomadakis & Sotirchos	$\mathcal{D}_{\text{eff}} = \varepsilon \left[\frac{\varepsilon - 0.037}{0.963}\right]^{0.661} \mathcal{D}_{ij}$	fibers	[74]	(2-6)
Mezedur *et al.*	$\mathcal{D}_{\text{eff}} = [1 - (1-\varepsilon)^{0.46}] \mathcal{D}_{ij}$	polygon	[75]	(2-7)
Zamel *et al.*	$\mathcal{D}_{\text{eff}} = \left\{1 - 2.76\varepsilon \cosh(3\varepsilon - 1.92) \left[\frac{3(1-\varepsilon)}{3-\varepsilon}\right]\right\} \mathcal{D}_{ij}$	fibers	[76]	(2-8)

2.3.3 Gas Permeability

The convective mass transport is an important contributor to the reactant transport to the CL [77]. The permeability of a porous medium is commonly determined by a simplification of the Darcy-Forchheimer equation reviewed in **Section 1.5.2**. By operating at low flow rates such that the Reynolds number is below 1, the inertial term becomes negligible. Since the pore Reynolds number in an operating PEM fuel cell is in the order of 10^{-4} [78], and the testing apparatus is in that range as well, the inertial effect is negligible. This simplifies **Equation (1-2)** into what is commonly known as Darcy's law:

$$\vec{v} = -\frac{k}{\mu}\nabla p \tag{2-9}$$

2.3.3.1 Experimental Methods

Based on **Equation (2-9)**, the determination of the permeability constant for a given sample is accomplished in two parts: first, controlling the flow of gas through the sample and, second, to measure the pressure difference between both sides of the sample. Since the concept of this design is relatively simple, multiple investigations into the measurement of the permeability constant were conducted using custom apparatus [77-79]. These designs had two common flaws: the flow chambers were short and the apparatus was not temperature controlled. Short flow chambers, which appear as a sudden expansion at the inlet and sudden contraction at the outlet, suffer from re-circulation of flow and can introduce significant source of error when measuring the pressures. While there is a low dependence on temperature in the determination of the permeability constant [81], an inhomogeneous temperature distribution will affect pressure measurements due to their interdependence in a closed system.

A Loschmidt Cell could be modified to determine the permeability coefficient as many of the same parameters are measured. In addition to the temperature control offered by this type of design, it is commercially available and have been used towards this end with an uncertainty typically under 3% [81].

2.3.3.2 Empirical Models

The overall pore structure controls the gas permeability of the GDL. Many models have been developed which use the porosity and, sometimes the fiber radius, to predict the permeability of different porous media. Some of these models are summarized in **Table**

2-3. These models are designed to operate on a certain pore structure, like random overlapping fibers. Many of the models rely on the assumption that the fibers are perfectly cylindrical. When the PTFE loading increases, altering the shape of the carbon fibers [64], these models begin to fail. In addition to fiber shape, permeability depends on size distribution, packing structure, inhomogeneity of materials like PTFE, and tortuosity [30, 81], which are not fully captured by any of the existing empirical models.

Table 2-3. Summary of some empirical models predicting the permeability constant of a porous material. Notes refer to the type of pore structure that the model was designed.

Model	Permeability Constant	Note	Source	Equation #
Kozeny-Carman Relation	$k = \frac{\varepsilon}{K_C}\left(\frac{V_{\text{pore}}}{S_{\text{pore}}}\right)^2$	general porous media	[83]	(2-10)
Kozeny-Carman with Mean Intercept Length	$k = \frac{r^2\varepsilon}{4K_C(\ln\varepsilon)^2}$	random overlapping fibers	[83]	(2-11)
Tomadakis & Sotirchos Random Walk	$k = \frac{\varepsilon r^2(\varepsilon - 0.11)^{2.785}}{8(\ln\varepsilon)^2(1-\varepsilon)^{0.785}[(1.785\varepsilon - 0.11]^2}$	fibers	[83]	(2-12)
Chen *et al.*	$k = \frac{4r^2\varepsilon^3}{150(1-\varepsilon)^2}$	spherical	[84]	(2-13)

NOTE: K_C = Kozeny constant; V_{pore}= Pore Volume; S_{pore} = Pore Surface Area; r = fiber radius

2.3.4 Summary

Numerous studies have been conducted investigating the transport mechanisms through the GDL. However, due to the technical challenge of the stress being applied in the same axis of the gas transport, novel methods have been attempted. Tehlar *et al.* used sintered steel, a porous material, to apply the compression and measure the through-plane permeability [85]. Hussaini *et al.* used a similar technique, except with a porous plastic plug [78]. Other studies have compressed the sample and then performed measurements with the sample unloaded. A summary of the research conducted is available in **Table 2-4** with a focus on using Toray samples because they are commonly reported on [62].

Table 2-4. Summary of gas transport studies through a GDL. If pore structure measurements are included, they have been identified.

Sample	PTFE (w/w)	Comp. (S/P)	Pore	Perm.	Diff.	Temp. Control	Source
TGP-H-090	0%	P	-	X (in)	-	-	[79]
TGP-H-120	N/A	P (porous plastic)	porosity	X	-	-	[78]
TGP-H-120	30%	S (1 stress load tested)	MIP	X (in)	-	-	[62]
TGP-H-060	0% 20%	P (sintered steel)	-	X	-	-	[85]
TGP-H-120	0% - 30%	P	-	X	-	-	[80]
TGP-H-090	5%	P	-	X	-	-	[18]
AvCarb GDS	5%	-	-	X	-	X	[81]
AvCarb GDS	5%	-	MSP	-	X	X	[69]
TGP-H-120	0% - 60%	S (multiple loads)	MSP	X	X	X	*THIS STUDY*

NOTE: PTFE = polytetrafluoroethylene treatment; Comp. (S/P) = Compression (Serial/Parallel); Perm. = Permeability; Diff. = Diffusion; Temp. Control = Temperature Control; MIP = Mercury Intrusion Porosimetry; MSP = Method of Standard Porosimetry; (in) = in-plane permeability; X = employed method.

2.4 Water Contact Angle

The principles of water contact angle are presented in **Section 1.6**.

2.4.1 Experimental Methods

2.4.1.1 *In-Situ* Measurements

There is a technical challenge when attempting to perform investigations to the *in-situ* water management of an operating fuel cell: it is a closed system and the inner workings are not visible. Some attempts have been made to observe the removal of water droplets using transparent flow channels [85, 86]. These visualizations can be complicated by the condensation that may arise on the flow channels, and they only have a top-down view. Water droplet contact angle information cannot be measured. An alternative method is to use neutron radiography to observe the movement of water and the physical effect of varying operating conditions, like clamping stress [87, 88]. However, very few facilities are available to perform this function. Further, neutron radiography has a limited spatial

resolution that is still not sufficient to visualize the water droplet movement in operating fuel cells.

2.4.1.2 *Ex-Situ* Measurements

A majority of the *ex-situ* experiments are on the formation and movement of water droplets on the surface of the GDL and MPL. The conditions of the water droplet can be dynamic or static, distinguished by whether the water droplet is in motion or not. The dynamic contact angle can be measured by the Wilhelmy Plate method or the sliding angle method [90]. In dynamic conditions, the droplet deforms such that there is an advancing and a receding angle corresponding to the direction of travel [91–94]. The static contact angle is measured by the sessile drop method and provides insight on the hydrophobicity, or hydrophilicity, of a material surface [94].

Wilhelmy Plate method uses a technique such that the sample is first submerged into a liquid and then slow removed. In both phases of the sample motion, the contact angle is observed [90, 93]. Parry *et al.* reported that the advancing angle was in the hydrophobic range and experienced near pure Cassie-Baxter conditions, while the receding angle experienced the opposite: hydrophilic contact angle and near pure Wenzel conditions [91]. This method does rely on the motion of the surface and not the motion of the water.

Sliding contact angle measurements start with a stationary water droplet on the surface as the stage that the sample is sitting on is slowly tilted until the water droplet moves [94]. The limitation of this technique is that it assumes only gravity but *in-situ* there are many forces acting upon it [39]. Numerical studies can overcome the limited interpretation of sliding angle [91, 92] by simulating the conditions more comparably found within the flow channels. Such numerical studies report that the higher contact angle will result in an earlier detachment and removal from the system [95].

Sessile drop method is accomplished by placing a small droplet of water onto the surface of the sample and then measuring the contact angle [94]. It is important to not use too large of a water droplet, under 20 μL, to prevent the weight of the droplet from affecting the results [93, 95, 96]. A relationship between static and dynamic contact angles have been investigated in numerical studies [98]. Due to the ease and this method being partially representative of *in-situ* conditions for the moments prior to the droplet removal, this method is utilized in this study.

2.4.2 Summary

A summary of selected literature investigating the water contact angle on the GDL surface is presented in **Table 2-5** with a focus on studies that involve compression and/or the solving of the Cassie-Baxter (or Wenzel) system of equations at varying PTFE loadings.

Table 2-5. Summary of studies into the water contact angle on the GDL surface, with emphasis on compression-based studies.

Sample	PTFE (w/w)	Comp. (S/P)	CA Method	Solve?	Source
Freudenberg H2315	0%, 10%	-	Wilhelmy	Cassie-Baxter	[91]
TGP-H-060	0% - 30%	-	Wilhelmy	Cassie-Baxter	[99]
TGP-H-120	30%	S (1 load tested)	Sessile Drop	-	[62]
TGP-H-090	5%	P	Sessile Drop	-	[18]
TGP-H-120	0% - 60%	S (multiple loads)	Sessile Drop	Cassie-Baxter	*THIS STUDY*

NOTE: PTFE = polytetrafluoroethylene treatment; Comp. (S/P) = Compression (Serial/Parallel); CA = Contact Angle; Solve? = Solve by system of equations

2.5 Commonly Employed Assumptions

Through the course of the literature review, numerous experimental studies employed assumptions to justify the methods. However, many of them, though reasonably sound, were not validated. A summary of the employed assumptions and corresponding studies are listed in **Table 2-6**.

Table 2-6. Summary table of assumptions used by various studies and whether they were validated.

Assumption	Source	Simply Stated	Validate?	
			Indirect	Direct
Thickness change, only porosity	[100]	x	no	no
	[78]	x	no	no
	[80]	x	no	no
Axial direction only (no radial expansion)	[79]	x	no	no
Manufacturer's specifications are accurate	[80]	-	no	no

2.6 Summary

Extensive studies have been conducted to better understand the gas transport through the GDL and the water removal from the GDL surface. However, much fewer studies have been conducted involving the variable compressed state of the GDL, which is typically found due to the inhomogeneity of the stresses found in the fuel cell unit assembly within a stack. To assist in our understanding, various empirical models have been developed to predict the transport properties of porous media but attempt to capture the complex interactions of multiple parameters into, in many cases, normalized volume (i.e. porosity). Furthermore, most studies do not include a comprehensive characterization of the individual samples tested. This is a necessary step given the inhomogeneity found within commercial GDL samples, which is likely the reason there are so many empirical models for the same phenomenon.

This present study is important because further research is required to promote the commercialization of PEM fuel cells. Concentration overpotential due to disruption of mass transport is significant, particularly at high current densities of the practical importance. A better understanding of the transport phenomena, and our ability to predict these phenomena, is critically urgent. This thesis study is focused on the development of a comprehensive understanding of the relation between pore structure, gas transport, and water droplet formation in the presence of a compressed GDL. By completing this research, the following contributions will be made:

1. Introducing a novel experimental method, serial compression of the same sample, that can be used to develop more robust and comprehensive empirical models for gas transport through a porous medium.
2. The pore structure characterization of the serially compressed GDL, such as porosity, pore size distribution, and mean pore radius, will reveal the evolutionary changes that occur while overcoming the issue of sample inhomogeneity.
3. Relating these changes in pore structures, while controlling other parameters like tortuosity and material interactions, the gas transport phenomena can be more directly compared to porosity and make initial assessments on the impact of the hydrophobic agent, PTFE.

4. Increase the understanding of the phenomenon of water droplet formation on a highly porous GDL and the responses from physical structural changes resulting from compression.
5. By increasing the understanding in these areas, the increased knowledge can be implemented into future numerical studies that can lead to a more optimized PEM fuel cell that can attain high current densities at useful cell potentials.

Chapter 3

Experimental Methods

The experimental methods employed in this thesis research are based upon the concept of serialized testing. There is a risk of damaging the sample throughout the testing, voiding any of the results that may have been obtained. The overall working assumption is that the random arrangement of carbon fibers in the carbon paper GDL make it near impossible to properly assess the relationship of the pore structure to fluid interactions and transport. By investigating the changes resulting from a series of compressions on the same sample, a deeper understanding on the effect of pore structure on gas transport and water droplet characteristics can be ascertained. As most of the testing requires two samples to be stacked, an investigation into finding similar samples must be first conducted. **Fig. 3-1** shows the flow of work. After each compression level, the sample undergoes five non-destructive tests: surface visualization, characterization of the pore structure, determination of the effective diffusion coefficient, determination of permeability, and water droplet contact angle measurements. All of these are *ex-situ* methods using available apparatus in our laboratory. The uncertainty of each experimental method is identified and quantified considering both bias and precision errors. All uncertainties are studied within 95% confidence intervals unless otherwise specified.

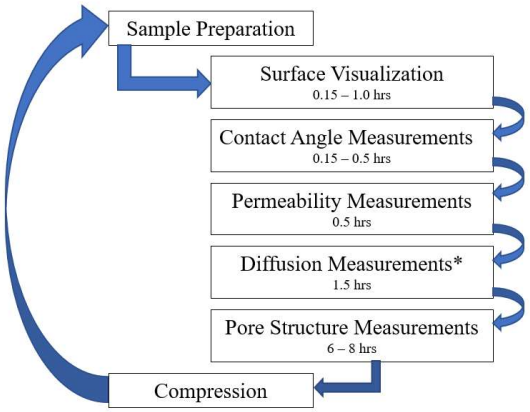

Fig. 3-1. Schematic of the workflow conducted in this research. *While diffusion measurements are included in this schematic, these measurements were completed in a separate run of the research.

3.1 Sample Selection

The random arrangement of carbon fibers in the carbon paper GDLs make it difficult to predict two adequately similar samples. Additionally, the PTFE treatment can be inhomogeneous [54, 55, 100, 101] and differ from the manufacturer's specifications. Toray TGP-H-120, with varying PTFE treatments, is the commercial GDL used throughout these investigations. While there are quite a number of GDL manufacturers with different brand names, and different fuel cell developers have their own preferences in GDL use, Toray TGP-H-120 has been used extensively in literature [36, 37, 45, 54, 61, 79, 100, 102, 103] allowing for these results to be better compared.

The intrinsic properties of the samples were measured primarily using standard methods. The thickness of the samples was measured using a disk micrometer (Fowler Electronic Disk Micrometer). The thickness of each sample was measured at least 10 times and averaged. The mass of each sample was measured using a digital scale (Sartorius ALC-210.4). The average diameter of each sample was measured by using a combination of a ruler and a digital image. By taking an image (12.0 MP camera on Samsung Galaxy S7) of both the sample and ruler together, the number of pixels could be counted between two opposing edges of the sample and scaled to a comparable length of pixels on a nearby ruler. A sample of an image used in diameter measurements can be seen in **Fig. 3-2**. Two measurements were taken for each sample, one in each of the cardinal axes and averaged. This method allows for greater sensitivity and resolution when relying on a ruler. With mass and dimensional data, the bulk density of each sample could be calculated.

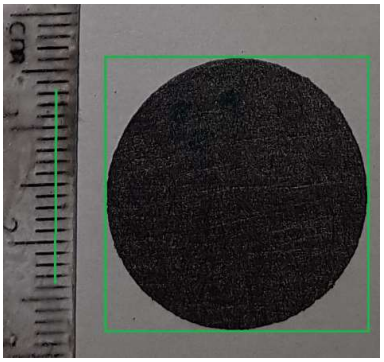

Fig. 3-2. An example of the procedure to determine the average diameter of a circular sample using image analysis.

Thermogravimetric analysis (TGA) would yield the most accurate determination of the PTFE content but this procedure is destructive and unsuitable for serialized testing. While using a die to cut the samples to identical circles, a simple measurement of the masses could reveal stark differences within the same larger sample source. A non-destructive means to confirm the PTFE loading could be calculated by comparing the bulk densities of the treated samples to the un-treated sample with a similar accuracy as found through TGA [105]:

$$(\text{PTFE content})_i\ [\text{mass/mass}] = 1 - \frac{\rho_{b,0}}{\rho_{b,i}} \tag{3-1}$$

where $\rho_{b,0}$ is the bulk density of an untreated sample and $\rho_{b,i}$ is the bulk density of a PTFE-treated sample, *i*. A summary of the physical properties of the samples used in these studies can be found in **Table 3-1**.

Table 3-1. Summary of the average properties and calculated PTFE content compared to manufacturer's specifications.

	Baseline	**Sample 1**	**Sample 2**	**Sample 3**
Expected PTFE (w/w)	0%	20%	40%	60%
Thickness [mm]	0.3775	0.3680	0.3635	0.3703
Diameter [mm]	23.1	23.0	23.2	23.1
Mass [mg]	69.2	86.5	105.9	169.1
Bulk Density [g·cm^3]	0.441	0.565	0.701	1.098
Calculated PTFE (w/w)	0.0%	21.95%	37.04%	59.84%

3.1.1 Uncertainty Analysis

The uncertainty of each individual measuring method is listed in **Table 3-2**. Most methods report an absolute error and, thus, relative errors are computed against the smallest recorded values to yield the largest possible relative error. The relative errors are then combined by taking the root-sum-square (RSS) and reveals that the uncertainty of the density calculations is < 0.71% and the uncertainty of the PTFE loading calculation is < 1.01%.

Table 3-2. Summary of uncertainties in different measurement methods.

Instrument/Method	Absolute Uncertainty	Maximum Relative Uncertainty
Electronic Disk Micrometer	0.0013 mm	0.35%
Ruler + Image for Diameter	0.1 mm	0.43%
Digital Mass Scale	0.05 mg	0.07%

3.2 Surface Visualization

In order to visualize changes to a sample undergoing compression, imaging techniques are often used: scanning electron microscope (SEM) and X-ray micro-computed tomography (CT). These techniques require very small samples to be effective and are not easily accessible. In this thesis research, an optical microscope (Zeiss Axio Zoom.V16) is used. At the maximum magnification, 260X, it is capable of resolving length scales around 1 μm, which is the low range of the domain of the carbon fiber diameters. At this magnification, the field of view is approximately 1 mm x 1 mm, which is the reported representative elementary surface area for GDL samples [55].

Consistent with the theme of serial testing, it is important to be able to find the same locations on the sample after subsequent compressions. Combined with some patience, some patterns of the surface structure, the relative positions of landmarks, are visible at lower magnifications. Once the circular sample is oriented properly, a higher magnification is used to visualize the surface microstructure. A sample series of such images can be viewed in **Fig. 3-3**.

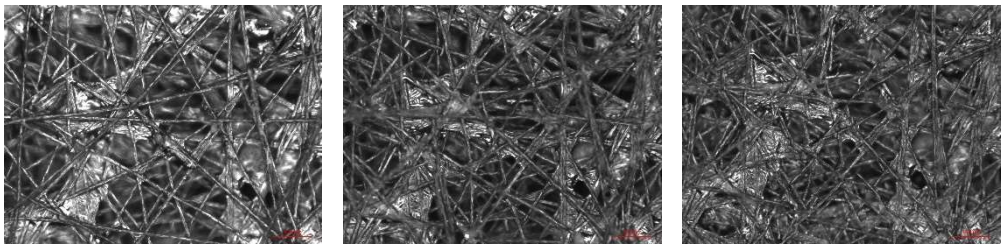

Fig. 3-3. Sample series of a sample with 37% PTFE treatment changing with from left-to-right: uncompressed, 0.117 residual strain, and 0.271 residual strain.

3.3 Compression

3.3.1 Principle of Residual Strain

To overcome the technical challenge of attempting to measure transport mechanisms in the same axis as compression and to measure surface phenomena where the load is applied, *ex-situ* experiments are the only feasible method to complete this task [106]. Tamayol *et al.* [80] and Aldakheel *et al.* [18] employed the method of initially applying a stress to a sample and then to test the samples once it was unloaded. The initial stress would always yield a permanent change to the thickness.

Strain is defined as the normalized change in length in response to a stress. All materials experience strain when subjected to a stress. When the carbon paper samples are compressed, they experience strain. However, when the stress is removed, the sample does not regain all of its original thickness. Some of the strain persists as a permanent deformation of the sample. This normalized permanent change in thickness is henceforth referred to as "residual strain". It is assumed that the structure of the residually strained sample is comparable to the structure when the GDL material is compressed *in-situ* at a corresponding, but always lesser, load.

Mason *et al.* had reported that 10 compressions were required to reach stability [46]. However, other studies [45] have suggested, that only a few compressions are required to achieve convergence of the residual strain in response to the same peak stress, as seen in **Fig. 3-4**. While increasing the number of compression cycles would not expect to significantly alter the experimental measurements, a minimum number of cycles would be desired to maintain a level of efficiency when testing.

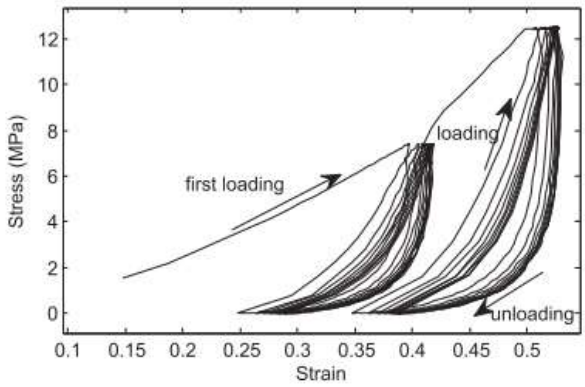

Fig. 3-4. Example of the stress-strain plot of a GDL sample when subjected to multiple sequential stresses [45].

3.3.2 Procedure

By applying a specific load onto the sample at a setpoint, two convergences of the resultant residual strain could be seen in **Fig. 3-5**. In addition to low time dependence on the setpoint time, the convergence reaches the uncertainty of the disk micrometer within 4 load cycles, which is also seen in Mason *et al.* [46].

In the operations of the hydraulic press (Carver Autoseries), a setpoint of load is inputted and applies it directly upon the sample. However, over a period between 45 – 60 seconds, there is a drift away from the setpoint. Once the drift is approximately 100 kg-f, the increment of measurement, below the setpoint, the press applies a corrective force to re-apply the setpoint load. In order to capture at least one correction back to the desired setpoint, a 90-second load time is used.

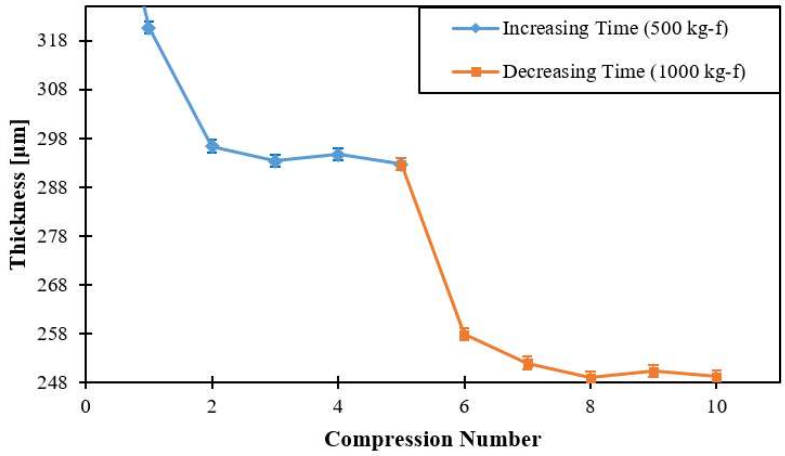

Fig. 3-5. Convergence of residual strain is achieved after 5 load cycles. At each compression, this sample was subjected to a peak stress of 7.3 MPa (blue) and 14.6 MPa (orange). The initial sample thickness was 375 µm. Increasing time at setpoint: 0.5, 1, 2, 5, 10 minutes. Decreasing time at setpoint: 12, 6, 3, 1.5, 0.75 minutes.

3.3.3 Observed Physical Changes

After each compression, the sample thicknesses were measured and the residual strain was calculated. A summary of the changes is shown in **Fig. 3-6**. This linear relationship is consistent with other reported observations in literature [44, 45, 106, 107] with respect to residual strain and increasing peak stresses and serves to validate the compression method. Additionally, it is apparent that the PTFE loading contributes to the strength of the carbon paper GDL by increasing the resistance to permanent deformation.

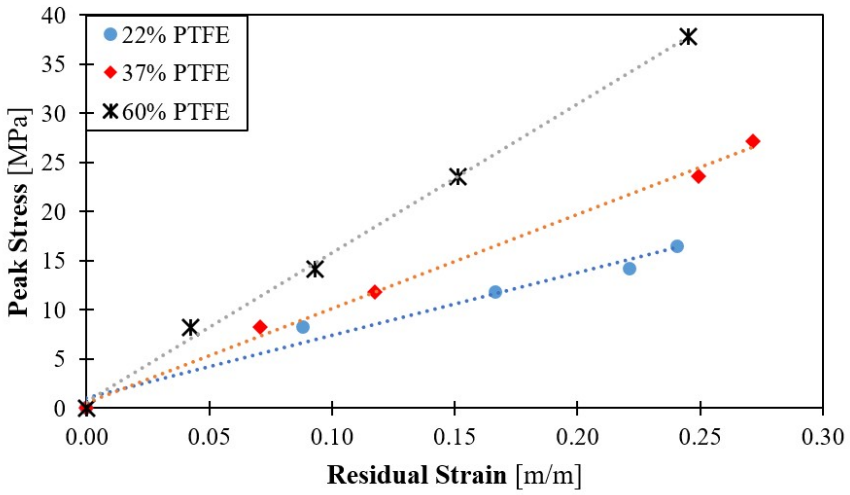

Fig. 3-6. Peak stress vs residual strain shows a linear trend.

3.3.4 Assumptions

As identified in the literature review, many past attempts at characterizing the different states of the GDL sample simply state their assumptions, often on the basis that they were used elsewhere [77, 99]. However, tracing the references back often leads to an article that does not explicitly test the validity of the assumptions. In this section, the working assumptions will be tested for their validity.

There are five parts to consider in this part of the investigation: (i) ensure good contact during the compression, (ii) the compression only causes a change in thickness (and not any of the other external dimensions), (iii) ensure that only the pore volume is changed with the thickness change, (iv) ensure the long-term stability of the residual

strain, and (v) confirm that other possible transport parameters are remaining relatively constant after each compression.

3.3.4.1 Validation of Good Contact

In order to investigate the uniformity of the stress distribution, while under load, a series of tests were conducted leveraging the GDL material responses to stress. This investigation involved three phases: (a) simultaneously compressing two samples with different PTFE loadings, (b) introducing a third sample (different PTFE loading from the other two) and simultaneously compressing them all under the same load, and (c) under the same load, compressing only one of the samples.

From **Section 3.3.3**, it was determined that the residual strain rate would decrease with increasing PTFE content. Additionally, when a new peak load is applied, the resulting residual strain would be observed as a step-change in the thickness. By compressing two different samples simultaneously, good contact would be assumed if both samples are compressed to equal thicknesses. Acknowledging that stress is the ratio of the applied load (force) and the cross-sectional area, by increasing the total area (by adding a third sample), the effective peak stress is lowered. However, if the other two samples are thinner than the new third sample, the third sample should be compressed to the same thickness as the other two. No further change to the thicknesses of the first two samples would be observed since they are now being subjected to a lower peak stress. The converse would also be true: reducing the number of samples to one would double the peak stress experienced by that sample. This is confirmed by the subsequent step change in thickness of that one sample.

3.3.4.2 Validation of Changes in Axial Direction Only

A popular assumption used in previous compression studies is that the compression only alters the sample in the same axis in which compression is occurring [79]. In other words, the sample does not expand radially after compression. This can be observed by carefully observing changes in the cross-sectional area, or the diameter of the circular samples, with increasing residual strain. If this assumption is false, it would be most markedly observed after the greatest strain. The average observed change to the average diameter of 3 samples was -0.27% change after a peak compressive stress of approximately 37.80 MPa, well above the typical stresses found *in-situ* [9].

3.3.4.3 Validation of Porosity Changes Only

Another common assumption is that the change in thickness of the GDL sample is solely from the loss of the air-occupied pore volume. Combined with the validated assumption that the sample is only compressed in the axial direction, as represented as a change in thickness only, and the mass of the empty pore space is negligible, it is reasonable to assume that the sample mass being conserved over successive compressions is a result of only a loss of the negligible pore space. The sample masses largely remained constant, 0.00% change from native to the last compression, with one sample experiencing a loss of 0.2%, or 0.2 mg. Of importance in the main study, the original baseline sample without PTFE treatment experienced significant loss of mass (14.4 mg or 10.4%) over the course of the investigation.

3.3.4.4 Time Study on Rebounded Thickness

Since the serial testing of the samples span over several hours, the stability of the residual strain must be observed over time. Three samples were compressed under the same conditions of the testing procedure (4 cycles on/off) and their thicknesses were measured over a period of 24 hours. While most samples experienced no appreciable change in thickness, within the uncertainty of the disk micrometer, it was noticed that the sample with the highest PTFE loading (60%) did regain about 4.2 μm (1.3%), however still within the standard deviation of measurements. This may be owed to strengthening of carbon fibers by the impregnation with PTFE. Carbon fibers are typically manufactured bound with a resin, or binder, for cohesion.

3.3.4.5 Serial Compression of the Same Sample

One of the primary working assumptions of this thesis research is that by using the same sample over successive compressions, parameters, like the tortuosity and material properties, would remain constant and, thereby, isolating the effect of changes in the pore volume with respect to gas transport properties and water droplet contact angle on the surface of the GDL.

Consistent with the conserved mass over the series of compressions, it is expected that the interactions between the fluids with the core of the sample being minimally affected. The fluids are still interacting solely with the PTFE and carbon fibers as, in the context of gas transport, courses through the sample and, in the context of water

droplets, interacting with the same surfaces though slightly altered after each compression.

Since tortuosity is typically calculated, and not measured, the validity of this assumption will be further explained in **Section 4.4.1**.

3.4 Pore Structure of the Gas Diffusion Layers

The method of standard porosimetry (MSP) is selected to measure the pore size distribution of the GDLs due to its wide range of measurable pore size, no deformation to the tested porous samples, non-poisonous working liquid, and good agreements with other methods. The Standard Porosimeter 3.1 manufactured by POROTECH (now MPM&P Research Inc. [109]) is utilized to test the samples automatically.

3.4.1 Principle of Standard Porosimetry

The MSP is developed based on the principle of capillary equilibrium [108, 109], which means that if two or more porous materials spend a sufficient amount of time in the same wetting liquid, they will achieve the same capillary pressures.

The MSP experimentally determines the relationship between the liquid volume in the test sample and liquid volume in the standard sample. The liquid distribution in the standard sample can then be expressed as a function of capillary pressure and is provided by the manufacturer. The capillary pressure can be expressed as the Young-Laplace equation [110]:

$$p_{\text{cap}} = -\frac{2\sigma \cos\theta}{r_{\max}} \tag{3-2}$$

where p_{cap} is the capillary pressure, σ is the surface tension of the liquid, θ is the wetting angle, and $r_{\max}$ is the maximum pore radius saturated with the wetting liquid. Since octane has a wetting angle of almost zero for all materials, and the maximum pore size of the test samples are the same as the standards, at that point in time. The relationship between the liquid volume in the test sample and the maximum pore radius can be established. By repeating this evaporating and measuring procedures, more data points are collected to generate the pore size distribution (PSD) curve for the tested sample.

On the other hand, the total pore volume, V_{pore}, of the test samples can be determined as follows:

$$V_{\text{pore}} = \frac{m_{\text{sat}} - m_{\text{dry}}}{\rho_{\text{liquid}}} \tag{3-3}$$

where m_{sat} is the total mass of the saturated sample, m_{dry} is the total mass of the dry sample, and ρ_{liquid} is the density of the test liquid, octane in the present case.

The bulk volume, V_{bulk}, can then be calculated. The porosity, ε, can then be defined as:

$$\varepsilon = \frac{V_{\text{pore}}}{V_{\text{bulk}}} \tag{3-4}$$

Furthermore, the pore surface area, S_{pore} can be calculated from the integral pore radius distribution curve by using the following equation [111]:

$$S_{\text{pore}} = 2\int_{r_{\text{min}}}^{r_{\text{max}}} \frac{1}{r}\frac{dV_t}{dr}dr \tag{3-5}$$

The mean pore radius, $\bar{r}_{\text{pore}}$, an extension of the concept of hydraulic radius, is given by [110, 112]:

$$\bar{r}_{\text{pore}} = \frac{V_{\text{pore}}}{S_{\text{pore}}} \tag{3-6}$$

3.4.2 Experimental Procedure

The test samples are first cut into disk-like shapes with a diameter of 23 mm using a die. 2 samples are stacked together as an individual test object so that the assembled test samples are thick enough to uptake sufficient liquid. Therefore, an adequate number of measurement points can be achieved to plot a relatively smooth PSD curve.

The thickness of the samples is measured directly by the micrometer. The diameters are measured using image analysis of the 2 widest parts of each sample and then averaged over 4 readings (2 readings for each of the 2 samples). Additionally, the compacted dry samples and two dry standard samples, are weighed separately by using the digital balance.

After preparing the test samples, this experiment is conducted in three major phases: (i) the test and standard samples are dried together in a vacuum tube, (ii) the test and standard samples are saturated with the octane, and (iii) the test and standard samples are systematically dried and weighed over time. In the first phase, the test and standard samples are heated up to 65 °C under a vacuum environment of about -1 atm. After half

an hour, the samples are free of any residual moisture and is assumed that the pore spaces are empty. The dry samples are weighed before being placed in another vacuum tube with an attached bulb to immerse the samples in octane. The immersion allows the test and standard samples to achieve capillary equilibrium while the vacuum removes any dissolved air in the octane and then the samples are placed into individual clamping devices and stacked. The assembled samples and clamping devices are placed under a normal force of 6.86 N, under which the samples will not be damaged and allow them to be kept in close contact. While in the heater, a small amount of octane evaporates from the test and standard samples, and a new capillary equilibrium is achieved. The heater is kept at 45 °C for 3 minutes, after which the heater opens and a mechanical arm moves the clamping devices with samples onto the digital scale. The digital scale weighs all 3 clamping devices with samples, then the bottom 2, then the bottom alone, and by the differences, the individual masses can be obtained and the evaporated liquid in each sample can be calculated over time, as seen in **Fig. 3-7**. This step is repeated about 60 times until the samples are completely dry and the mass no longer changes with subsequent readings.

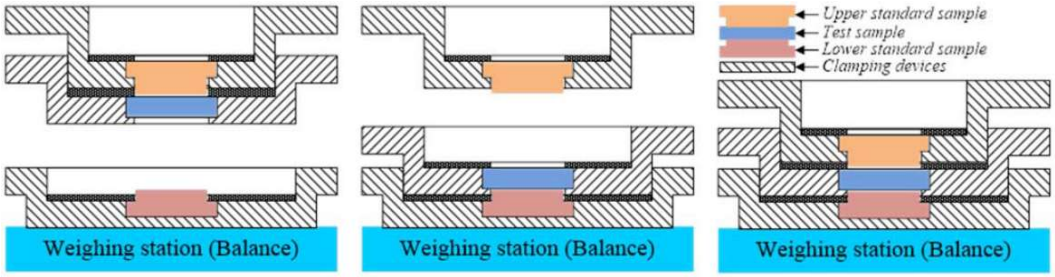

Fig. 3-7. Sequence of mass readings are determined by the differences between each subsequent reading to determine the liquid mass of the octane remaining in each sample [5].

3.4.3 Uncertainty Analysis

As the same instruments are used in previous measurements, the uncertainty of each individual measuring method is listed in **Table 3-2**. Most methods report an absolute error and, thus, relative errors are computed against the smallest recorded values to yield the largest possible relative error. The relative errors are then combined by taking the root-sum-square (RSS) and reveals that the uncertainty of the porosity < 1.01%. Additionally, the relative measurement uncertainty of the PSD also depends on the uncertainty of the standard sample which is < 1% according to Volfkovich and Sakars

[110]. Therefore, the MSP used in this study is suitable for the GDLs and the measurement of uncertainty is acceptable.

3.5 Effective Diffusion Coefficient

The closed-tube method (also known as a Loschmidt Cell) is employed in this study to measure the effective diffusion coefficient due to its high accuracy, ease of operation, and feasibility of controlling experimental time and temperature. A Loschmidt Cell utilizes a long tube closed at both ends separated in the middle by an opening mechanism. Initially, the top and bottom chambers are filled with two different gas species and, when the mechanism opens, the diffusion commences. Subsequently, the concentration of one gas species is measured and recorded by a sensor. The composition change is a function of time after a defined period of diffusion. In this thesis research, oxygen gas diffusion into nitrogen gas is studied by an oxygen sensor installed inside the nitrogen chamber.

3.5.1 Principle of the Loschmidt Cell

The development of the diffusion theory is crucial to calculating the diffusion coefficient by analyzing the signals provided by the oxygen sensor in the Loschmidt Cell. The diffusion process in the chamber follows Fick's Second law of Diffusion:

$$\frac{\partial C}{\partial t} = \mathcal{D}\left(\frac{\partial^2 C}{\partial x^2} + \frac{\partial^2 C}{\partial y^2} + \frac{\partial^2 C}{\partial z^2}\right) \tag{3-7}$$

where C is the concentration of a gas species in mol·m^{-3}, t is the diffusion time in s, $\mathcal{D}$ is the diffusion coefficient in m^2·s^{-1}, and x, y, and z are the cardinal spatial dimensions.

This problem can be simplified to be one-dimensional with a sufficiently large cross-section to the tube. This will reduce Fick's Second Law to:

$$\frac{\partial C}{\partial t} = \mathcal{D}\left(\frac{\partial^2 C}{\partial x^2}\right) \tag{3-8}$$

According to the experimental setup and procedures, the initial conditions are:

$$C = \begin{cases} C_{\text{top}} = 0 & for\ 0 < x < {}^{L}/_{2} \\ C_{\text{bot}} = C_{\max} & for\ {}^{-L}/_{2} < x < 0 \end{cases} \tag{3-9}$$

where C_{top} and C_{bot} represent the initial concentration of oxygen in the top and bottom chambers, respectively. Additionally, the experimental setup is completely closed such that there is no diffusion occurring at the ends ($x = \pm \mathrm{L}/2$).

The solution of the diffusion equation for these initial and boundary conditions are provided by Crank [32]:

$$C(x,t) = \frac{C_{\max}}{2}\,\mathrm{erfc}\left(\frac{x}{2\sqrt{\mathcal{D}_{\mathrm{eq}}t}}\right) \tag{3-10}$$

This equation is based on a semi-infinite-length model and is used in this experiment to obtain the equivalent diffusion coefficient, $\mathcal{D}_{\mathrm{eq}}$. This is achieved by fitting this solution to the experimental data as shown in **Fig. 3-8**.

The resistance network as shown in **Fig. 3-9** helps to obtain the effective diffusion coefficient of the gas pair in the porous samples. The equivalent diffusion resistance is equal to the sum of the diffusion resistances in the chamber and that in the sample. Diffusion is the most dominant transport mechanism in these chambers, and convection effects are negligible. The fluid is considered to be motionless.

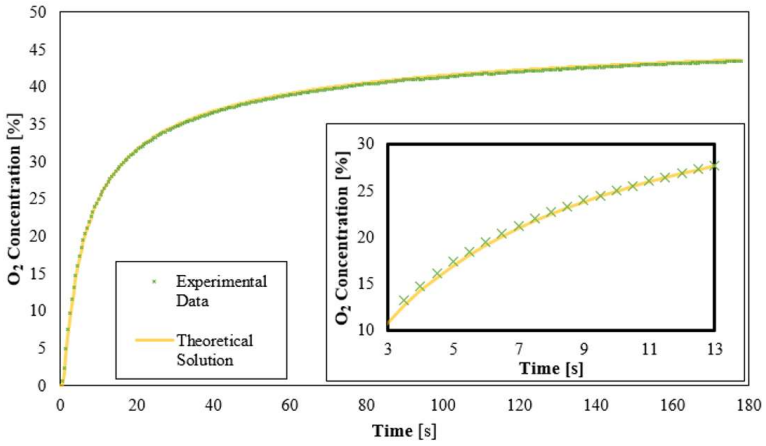

Fig. 3-8. Sample of fitting the experimental data to Crank's 1-D solution. *Inset*: the oxygen sensor is more reliable between 10% and 30% oxygen concentrations and the fit is most important in this range.

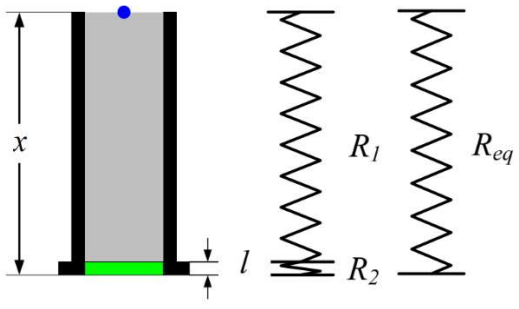

Fig. 3-9. Schematic of the resistance network to diffusion.

The equivalent diffusion resistance in the chamber is:

$$R_{\mathrm{eq}} = \frac{x}{\mathcal{D}_{\mathrm{eq}} A} \tag{3-11}$$

where R_{eq} is in $\mathrm{s \cdot m^{-3}}$, $\mathcal{D}_{\mathrm{eq}}$ is the equivalent diffusion coefficient in $\mathrm{m^2 \cdot s^{-1}}$, A is the cross-sectional area, and x is the location of the oxygen sensor from the bottom of the test sample. Meanwhile, the resistance due to the diffusion in the chamber is:

$$R_1 = \frac{x - l}{\mathcal{D}_{ij} A} \tag{3-12}$$

where l is the thickness of the sample in m. And, finally, the resistance due to diffusion in the porous GDL sample is:

$$R_2 = \frac{l}{\mathcal{D}_{\mathrm{eff}} A} \tag{3-13}$$

where, $\mathcal{D}_{\mathrm{eff}}$ is the effective diffusion coefficient of the sample.

By applying resistance network theory for a series of resistors, the effective diffusion coefficient of the GDL sample becomes:

$$\mathcal{D}_{\mathrm{eff}} = \frac{l}{\frac{x}{\mathcal{D}_{\mathrm{eq}}} - \frac{x - l}{\mathcal{D}_{ij}}} \tag{3-14}$$

3.5.2 Experimental Set-Up

A Loschmidt Cell consists of two chambers separated by a sliding gate as shown in **Fig. 3-10**. The top chamber and bottom chamber with an interior length and diameter of 42.5 cm and 3.8 cm are used to hold nitrogen and oxygen gases, respectively. The N_2 and O_2 gases can be separated or connected by the sliding gate made of a non-porous stainless steel. Two mass flow controllers (Omega, Model FMA-5508) with a flow capacity of 0-500 SCCM are used to control the flow rate of N_2 and O_2 during the calibration and experimental processes. An oxygen sensor (Pyro Science OXB50-HS) is used to measure the oxygen concentration in the oxygen-nitrogen binary mixture. The jacketed optical fiber probe with a diameter of 300 μm is installed in the top chamber as shown in **Fig. 3-10**.

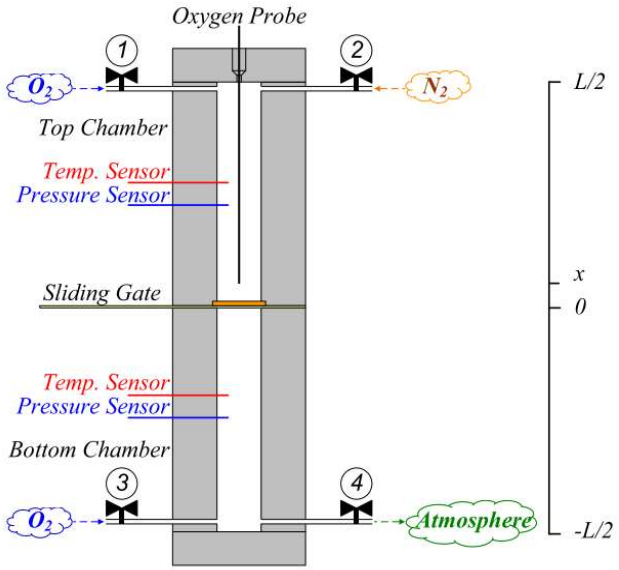

Fig. 3-10. Schematic diagram of the functional components of the Loschmidt Cell where *x* is the distance of the sample to the oxygen probe [5].

3.5.3 Experimental Procedure

The typical calibration and experimental processes, maintained at 25 °C, can be implemented by following eight steps:

1. Close Inlet 3, and open the sliding gate;
2. Inlet 1 and 2 is open and filled with O_2 and N_2 gases with a flow rate of 500 SCCM for 15 minutes while outlet 4 is opened to expel the originally existed gas in the chambers (calibration of 50% O_2);
3. Close Inlet 1, and fill the chambers with N2 gas through Inlet 2 for another 15 mins (calibration of 0% O_2);
4. Close the sliding gate, and open inlet 2 and inlet 3 to fill N_2 and O_2 gases into the top and bottom chambers, respectively;
5. Purge these gases in each chamber for 20 minutes;
6. Close all of the valves;
7. To keep the pressure inside the diffusion cell at atmosphere pressure, both valves 1 and 4 are opened for 2 seconds and then closed; and
8. The sliding gate is set to be opened smoothly so that the diffusion starts, and the temperature, pressure, and O_2 concentration changes are monitored and measured with sensors and recorded by the computer over a period of 3 minutes.

3.5.4 Uncertainty Analysis

The uncertainty of each measuring apparatus is outlined in **Table 3-3.** The uncertainty analysis indicates that the uncertainty in the results is most affected by the experimental time, probe location, and number of samples stacked. To minimize the relative uncertainty, the probe location is set to approximately 10 mm above the sample and the data points with a concentration of 10-30% are selected for the curve fitting.

Table 3-3. Uncertainty of individual measurements for Loschmidt Cell.

Instrument/Method	Absolute Uncertainty	Relative Uncertainty
Oxygen Sensor	0.02% O_2 @ 1% O_2 0.2% O_2 @ 20% O_2	2.0% @ 1% O_2 1.0% @ 20% O_2
Thermocouple	0.2 °C	0.80%
Pressure Sensor	30 Pa	0.03%
Flow Controller	-	1.5%

3.6 Permeability of the Gas Diffusion Layers

3.6.1 Principle of Permeability Measurements

The gas permeability of the porous electrode is determined by using the Darcy-Forchheimer law, **Equation (1-2)**. However, the pore Reynolds number for air in the PEM fuel cell electrodes is in the order of 10^{-4} [81] and it is also true in the current experimental setup. Therefore, the inertial effect is negligible and a simplified Darcy's law is valid for this study. The general form of Darcy's law is:

$$\vec{v} = -\frac{k}{\mu}\nabla p \tag{3-15}$$

The superficial velocity is defined as follows:

$$\vec{v} = \frac{Q}{A} = \frac{\dot{m}R_{\text{igl}}T}{AMp} \tag{3-16}$$

where Q is the volumetric flow rate in $m^3 \cdot s^{-1}$, $\dot{m}$ is the mass flow rate in $kg \cdot s^{-1}$, R_{igl} is the ideal gas constant in $J \cdot kmol^{-1} \cdot K^{-1}$, T is the temperature in K, A is the cross-sectional area of the samples in m^2, and M is the molecular weight of the gas in in $kg \cdot kmol^{-1}$. By combining **Equations (3-15)** and **(3-16)** and then integrating from the inlet pressure, p_{in}, to the outlet pressure, p_{out}, across the thickness, Δx, of the test porous sample, Darcy's law yields:

$$k = \frac{2\mu RT\dot{m}\Delta x}{AM(p_{\text{in}}^2 - p_{\text{out}}^2)} \tag{3-17}$$

The permeability tests are repeated at least five times under each condition, and the standard deviation is typically within 1-2% for the GDL samples.

Due to the relationship between superficial velocity, and in turn the flow rate, to the pressure gradient in **Equation (3-15)**, a linear profile in a plot comparing the two would internally validate the assumption of negligible inertial effects. This is observed as seen in some sample data provided in **Fig. 3-11**.

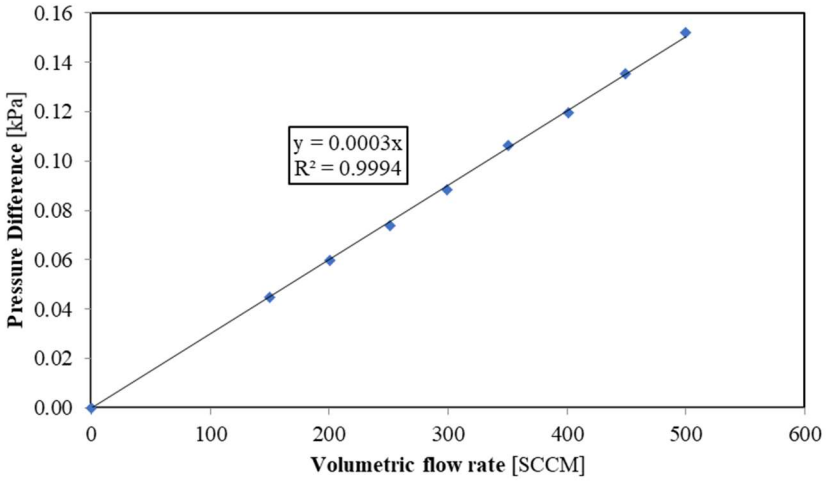

Fig. 3-11. Sample permeability data of the TGP-H-120 sample with 37% PTFE after 11.80 MPa peak stress. The linearity of the results validates the assumption of negligible inertial effects.

3.6.2 Experimental Set-up

Figure 3-12 shows the experimental setup used to measure the permeability of the electrode. The electrode samples are placed between two gas chambers. The interior length and diameter of the two chambers are 42.5 cm and 3.8 cm, respectively. The cross-sectional area of the tested samples is 3.14 cm^2. The oxygen gas with a purity level of 99.99% is used as the test gas. The gas is introduced into the top chamber through valve #1, forced to pass through the samples, and expelled to the ambient atmosphere through valve #2. Two pressure sensors and thermocouples are installed in both chambers to measure the pressure and temperature of the gases, respectively. The flow meter is employed at the inlet in order to control the mass flow rates of the supplied oxygen gas.

It should be noted that the sample diameter is smaller than the chamber diameters. This was to allow the same sample to be used in all but the diffusion

measurements (**Section 3.5.2**). The sample holder was designed based on the original sample holder and rapidly prototyped using ¼" thick clear acrylic and a laser cutter (Epilog Mini 24). The diameter of the hole opening where the samples sit is 20 mm. The sample holder can be seen in **Fig. 3-13**. The effect on the pressure difference, without a sample, in the setup required the use of a correction when performing the permeability measurements for the samples. This pressure difference correction, only 12.2 Pa (within the uncertainty of the pressure measurements), was applied to each pressure difference measurement based on a resistor-in-series network.

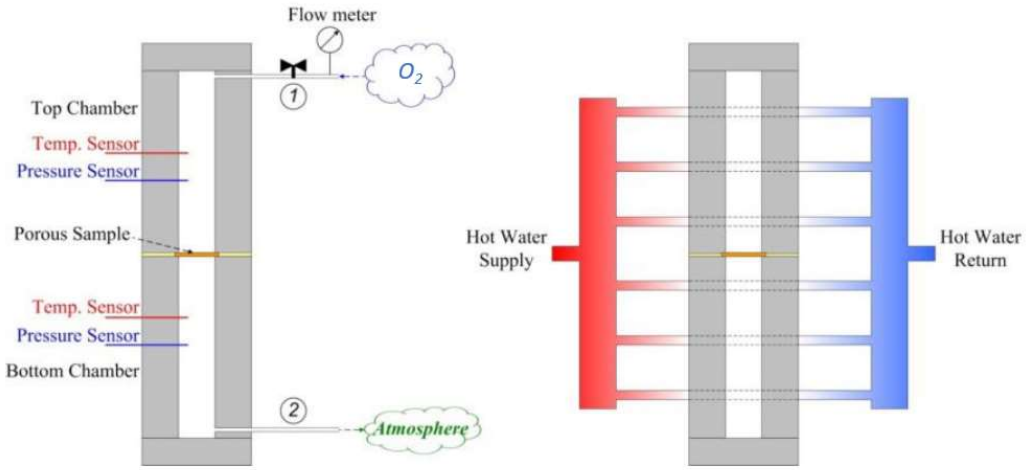

Fig. 3-12. Schematic of the experimental setup for gas permeability measurement. Adapted from [81].

Fig. 3-13. Prototype of a sample holder for a smaller sample in permeability measurements.

In this study, the temperature at which the permeability is measured is controlled by a water loop as shown in **Fig. 3-12**. A thermal bath (Thermo Fisher Scientific) is used to maintain the desired temperature with an accuracy of 0.2 °C. Thermocouples are located in both chambers in order to ensure temperature uniformity throughout during the test.

3.6.3 Experimental Procedures

A leak-check is performed before each experiment, and the experiment is conducted under predetermined operating conditions. The measurement procedure for each sample can be generalized into the following steps:

1. The temperature of both chambers is set 25 °C;
2. The inlet valve is opened and the chambers are filled with the oxygen gas;
3. The filling process lasts for more than 3 minutes with a flow rate of 500 SCCM;
4. After the flow is stabilized, the pressure and temperature of both the top and bottom chambers are recorded; and
5. Reduce the flow rate in increments of 50 to 100 SCCM, and repeat step 4 at least eight times.

Since in the PEM fuel cells, the mass transport of oxygen in the cathode is much slower than that of hydrogen in the anode, and the cathode process is more important in PEM fuel cell performance [113], only the permeability for oxygen is measured in this study.

3.6.4 Uncertainty Analysis

The measuring apparatus used in the permeability measurements is the same as the Loschmidt Cell and the individual sources of uncertainty can be found in **Table 3-3**. Since the pressure differences are being calculated, the greatest source of uncertainty is coming from the pressure sensors. To minimize the impact of the uncertainty of the pressure difference, the incremental reduction in flow rate (step 5), is determined depending on the initial pressure difference in response to a flow rate of 500 SCCM. If the initial pressure difference is less than 0.70 kPa, then smaller increments were used to minimize the uncertainty of the final results.

3.7 Water Droplet Contact Angle

3.7.1 Principle of Water Droplet Contact Angle Measurements

When a droplet of water encounters a surface, one of two mutually-exclusive phenomena will occur: the water will spread out over the surface or the droplet will maintain its structure on the surface. This is determined by the interaction of the surface energies between the water droplet and the surface the droplet interacts. This is often characterized by Young's Equation (see **Equation (1-3)**). However, this assumes that the surface that the water is interacting with is smooth and homogeneous, which the GDL surface is not. Sometimes a roughness coefficient is included to offset the assumption of smoothness, as, in any material, it is never perfectly smooth.

To overcome the limitation of Young's Equation, other non-analytical formulations have arisen. One of which is the Cassie-Baxter equations (see **Equation (1-4)**). Similar to the Cassie-Baxter equation is the Wenzel equation, where it is assumed that there is no interaction with air (f_{air} = 0). These formulations do not require a correction for the roughness [27].

3.7.2 Experimental Set-up

The experimental setup, as shown in **Fig. 3-14**, consists of a digital camera, software for calculating the apparent contact angle, and a dispenser for generating droplets with appropriate radii provided by Ramé-Hart Instrument.

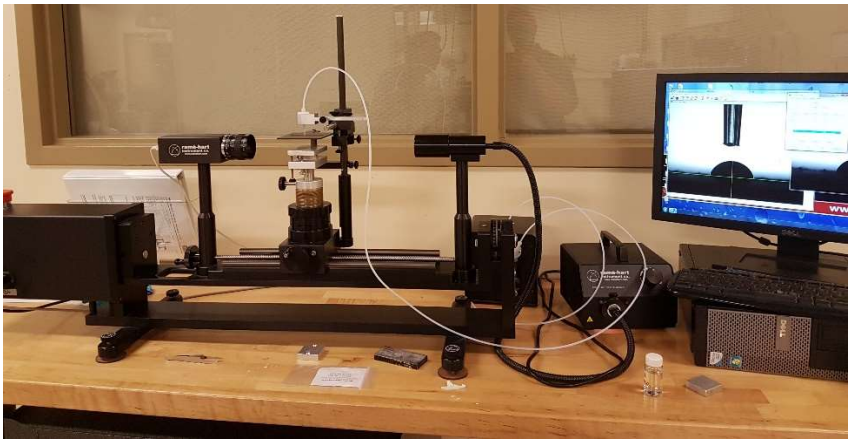

Fig. 3-14. Goniometer experimental setup for water contact angle measurements.

3.7.3 Experimental Procedure

Once the sample is placed on the stage, a small droplet of de-ionized water is placed onto the surface. The droplet size can vary, but to prevent the impact of larger droplets penetrating deeper into the sample, droplet sizes of 10 – 15 μL were used in this study. Using the software, the boundaries of the droplet are set the software then measures the apparent contact angle on the left and right side of the water droplet via image analysis as seen in **Fig. 3-15**. For each sample, 10 measurements are recorded from at least 4 different locations on each side of the sample.

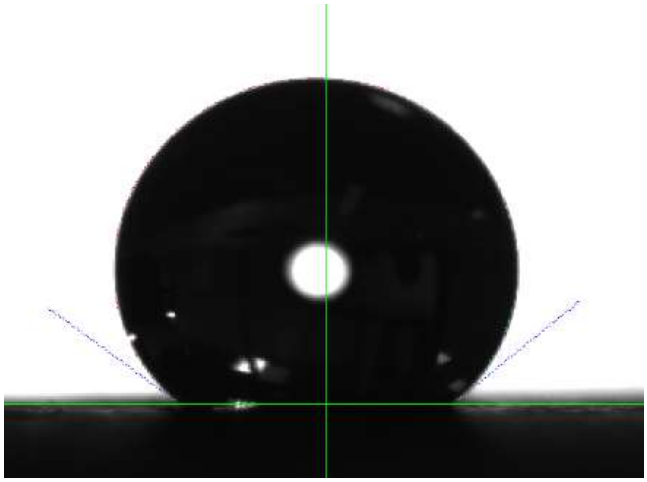

Fig. 3-15. Sample of the contact angle measurements by the goniometer. The horizontal green line represents the surface and the observed angles, as represented by the blue lines, are measured at the intersection of the water droplet to the surface.

Chapter 4

Results and Discussion

In this chapter, a carbon paper GDL is experimentally investigated through a series of compressions and is assessed for changes to its morphology, gas transport properties, and water droplet characteristics. Comparison studies are conducted with samples with varying PTFE loadings, from 0% to 60% (mass/mass). By isolating the effect of changing porosities, the results obtained from these studies are used to explain the phenomena found inside of a traditional PEM fuel cell.

4.1 Physical Analysis of the Native GDL samples

PTFE loadings, porosities, and pore size distributions of the native, or uncompressed, Toray TGP-H-120 samples are analyzed to establish their baseline properties. Preliminary correlations are also proposed to assist future numerical studies incorporating advanced mass transport models.

Other studies have attempted to develop correlations between PTFE loading and porosity [63, 89, 112]. These models are linear and are typically predictive within a narrow range of PTFE loading. **Fig. 4-1** compares the experimental data to these models. While true that within a narrow range, the relationship does appear to be linear, physically-speaking, it should not. This apparent linear correlation from the empirical models arises from the constrained PTFE range that was tested, < 30% PTFE [114], 40% [64], or proportional to the density of PTFE [90]. With greater PTFE loading, it is

expected that the PTFE should further surround the individual fibers, effectively increasing the carbon fiber diameter. This near linear change would cause a linear change to the pore radius. It should be noted, however, given the range of PTFE loading commercially available (0% - 60%), a cubic correlation with the available data, not shown, is equally as accurate (R^2 = 1) and, unless even greater PTFE loadings could become available (e.g. 75%), cannot be investigated further.

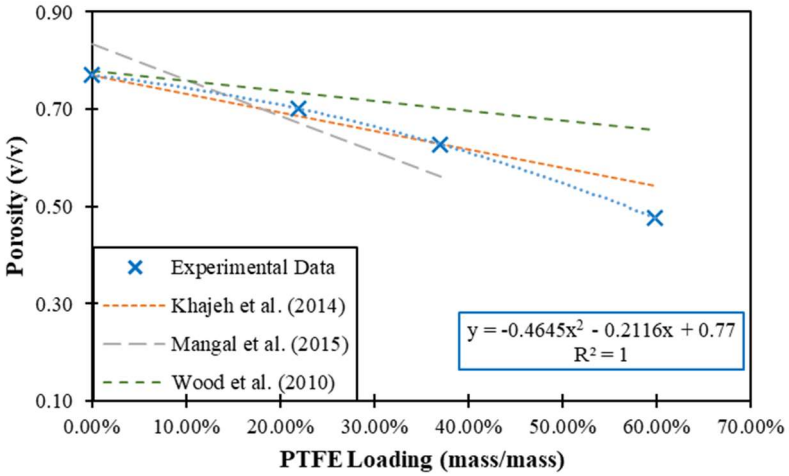

Fig. 4-1. Correlation between PTFE loading and Porosity of TGP-H-120 samples. Empirical models (derived from data of 40% PTFE or less) provided for comparison.

Based on a stronger linear relationship of mean pore radius squared to the porosity, a non-dimensionalized value for pore volume, as seen in **Fig. 4-2**, it is a reasonable assumption that the pores are cylindrical, instead of spherical. This approximate linear relationship can serve to validate the working assumption of cylindrical pores in the MSP.

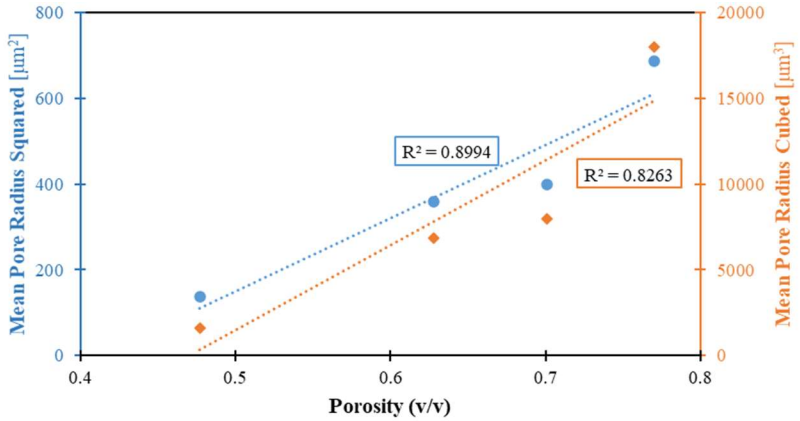

Fig. 4-2. Determining a linear relationship of porosity to mean pore radius squared or cubed.

An investigation into the pore size distribution of the native GDL samples is highlighted in **Fig. 4-3**. The focus is what pore radius contributes most of the pore volume in any of the given samples. Note that the x-axis is in a log-scale. The native sample of 0% PTFE is marked with a narrow peak corresponding to a pore radius of 2.2 μm. The addition of PTFE, though, initially broadens the peak. For both the 22% PTFE and 37% PTFE samples, the peak occurs at a pore radius of 2.3 μm and have similar profiles. The broadening of the peaks may be due to the method of PTFE loading by the manufacturer. Depending on the PTFE treatment process, PTFE may preferentially get deposited towards the surfaces of the GDL [52, 55] as well as large collections of pores. This would leave many of the pores in the core region of the GDL largely unaltered, resulting in the broadening of the peak and a slight upward shift. The 60% PTFE sample, however, sees a marked shift towards a smaller peak pore radius of about 1.7 μm. With greater PTFE loading, the process may have allowed for greater penetration of the PTFE into the core regions of the GDL thickness, thereby reducing the larger pores.

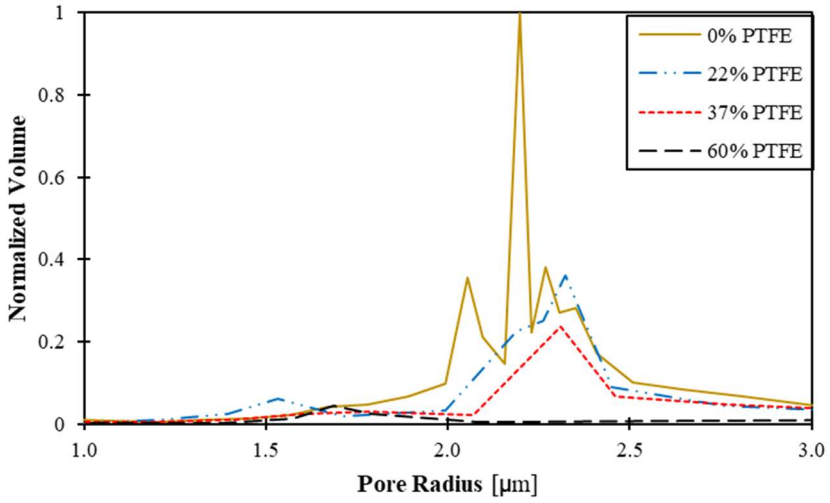

Fig. 4-3. Peak pore radii and distribution compared to the volume (normalized to the peak volume in the 0% PTFE sample). *Note*: the full range of measured pore radii have been truncated to show an enhanced distinction of the peaks.

A final practical relationship, detailed in more depth in **Section 4.5.2**, is a correlation between the PTFE loading and mean pore radius. The establishment of this relationship, coupled with another relationship into the change in mean pore size in response to compression, could be used to enhance mass transport modeling in numerical fuel cell simulations. This correlation is found in **Fig. 4-4**. Again, the narrow range of the

available PTFE loadings on the GDL substrate makes it difficult to establish a clear linear or non-linear relationship. However, since PTFE loading is a mass relationship, with a direct relationship to the total volume of the PTFE being added to the cylindrical carbon fiber, there is a linear relationship between the added volume and the fiber diameter. This increased fiber diameter would, in turn, cause a corresponding reduction in the pore radius.

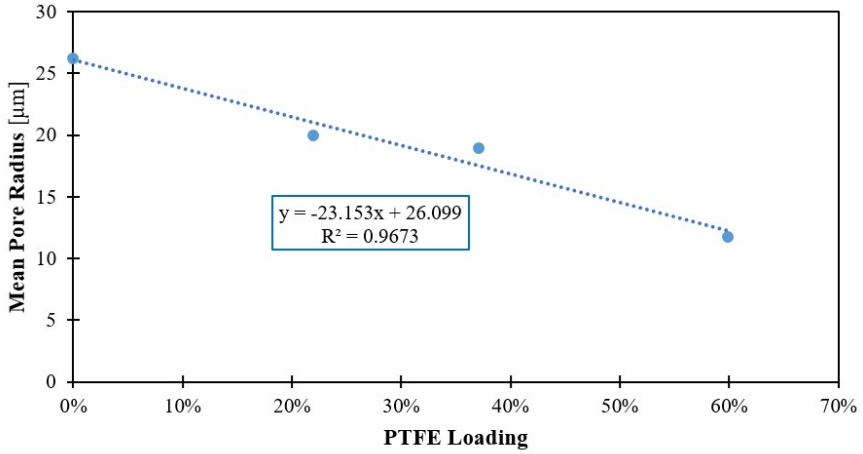

Fig. 4-4. A correlation between the PTFE loading and Mean Pore Radius. This correlation can be used in future numerical studies

4.2 The Baseline PTFE Loading

Before further results are provided, it is important to highlight that the baseline PTFE sample (0% PTFE) did not survive the series of compressions. While it was not evident after the first compression, it became very clear by the third compression that one of the principle working assumptions of the serial testing was violated: only porosity changes with compression. The mass of the sample decreased from 138.4 mg (native) to 137.8 mg to 132.1 mg and then to 124.0 mg after the third compression at approximately 14 MPa. By the third compression, the 0% PTFE sample had decreased in mass by 10.4%. It also presented visually, in **Fig. 4-5**, after the saturation with octane during the sample preparation to determine the pore size distribution.

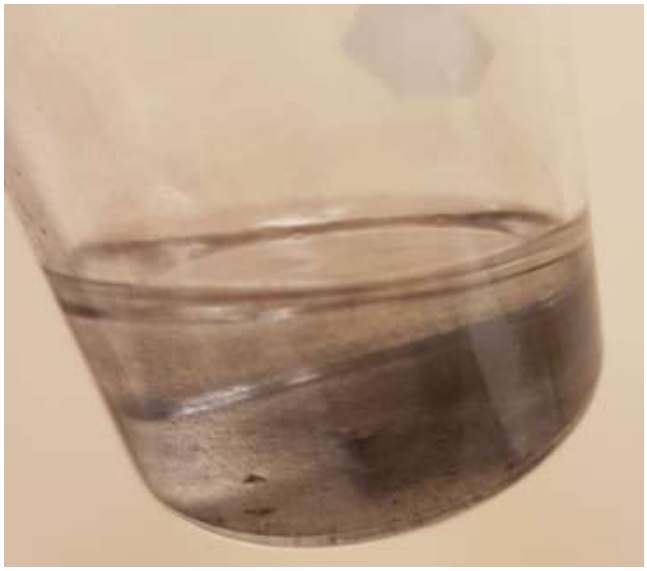

Fig. 4-5. Carbon particles present in octane after the preparation of the 0% PTFE sample for the Method of Standard Porosimetry.

Furthermore, these significant changes to the morphology of this GDL sample were confirmed in the observed changes in the pore size distributions. **Fig. 4-6** shows the evolving pore size distribution with each further compression. Contrary to expectations, whereby compressions should yield a trend towards smaller pores, further compressions on the 0% PTFE sample revealed the opposite outcome. Increasing compressions resulted in the formation of pore radii in the range of 1 – 100 μm.

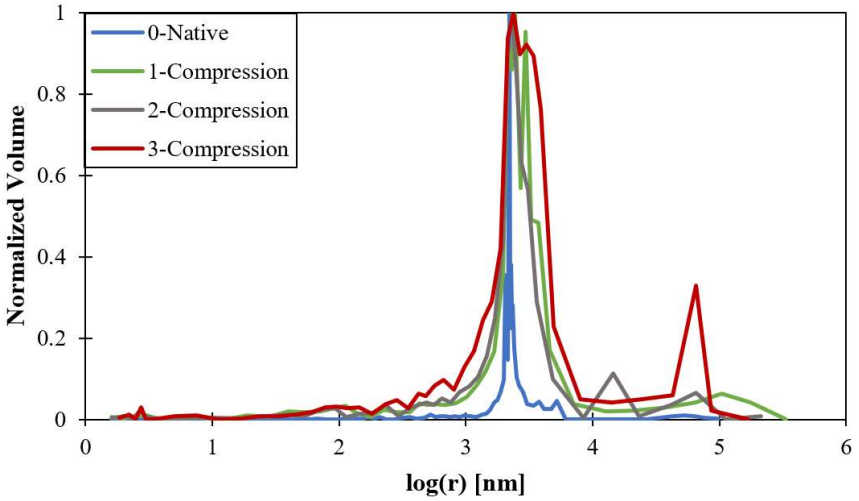

Fig. 4-6. Pore Size Distribution for the 0% PTFE sample with each additional compression. Note the evolution of larger pores with each subsequent compression.

This unexpected trend is likely owed to the added strength that the manufacturer's post-processing with PTFE gives to the originally raw GDL material. In addition to surrounding the fibers of the carbon paper, protecting the fibers from direct physical damage, the PTFE can also behave as an adhesive between the individual strands that the carbon fibers are composed. The damage to the fibers, and the resulting carbon residue released from the GDL, may attribute to the lower comparative performance of untreated GDL in PEM fuel cells, *in-situ* [115], in addition to the enhanced water management.

This example serves to highlight the risk that is involved with serial testing, in general. The damage to this PTFE condition voided the series of results collected from it. For this reason, the 0% PTFE loading condition is excluded from all further analyses.

4.3 Morphological Changes with Compression

The compression of the samples produces irreversible changes to the surface and the pore structure.

4.3.1 Surface Changes

Visual inspection of the surface of the samples after each subsequent compression was accomplished using an optical microscope (Zeiss Axio Zoom.V16). The overall accessibility and ease of use allowed locating the same point on the sample at 260X magnification possible. The evolution of the surface changes is shown in **Fig. 4-7**.

It is evident, and expected, that following the compression, there would be some breakages and displacement of individual fibers, this is also observed *in-situ* [9]. After the first compression, however, many of these changes are difficult to spot. However, these permanent physical changes to the surface do become apparent after each subsequent compression. Though, notably, the larger accumulations of carbon fibers and binder and/or PTFE helped to keep some of the larger microstructures intact despite peak stresses between 16.50 MPa (for the 22% PTFE sample) and 37.80 MPa (for the 60% PTFE sample).

Another significant change, though more noticeable at the higher PTFE loadings, is the encroachment of the underlying GDL sample towards the surface. While the precise changes cannot be determined, given the very narrow depth of field of the

microscope, the underlying material starts to become more in-focus with the surface materials by the final compression.

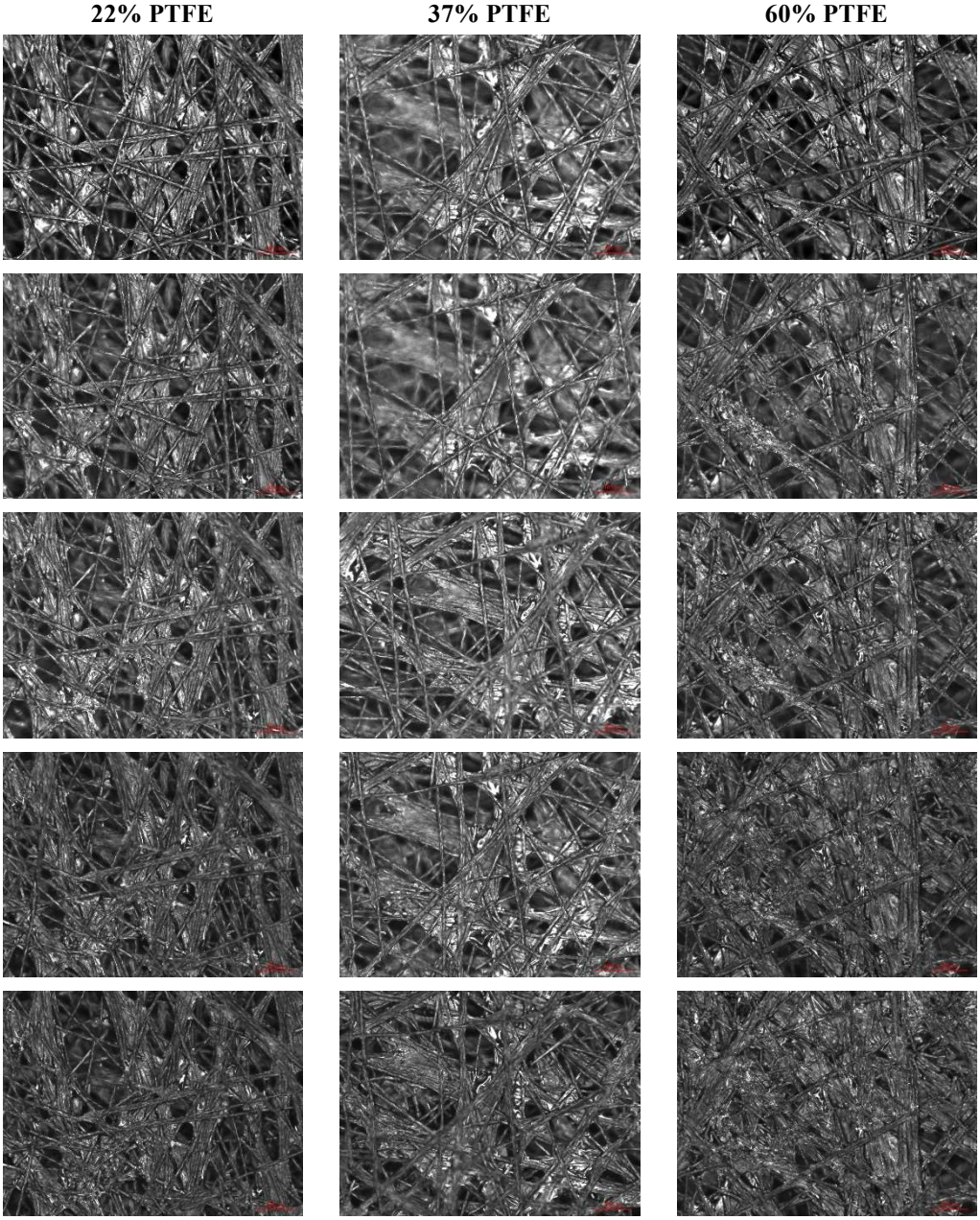

Fig. 4-7. Evolution of surface changes to the GDL samples of varying PTFE loadings from the native condition up to a peak nominal stress of 37.80 MPa for the 60% PTFE sample. All images were taken at 260X magnification. Note the breakages of some of the fibers after compression as well as the appearance of core fibers of the GDL approaching the surface resulting in reduced roughness.

Finally, after the last compression, some smoothing of the top carbon fiber strands, most visible in the 60% PTFE sample, is visible. However, despite a similar residual strain, the 22% PTFE sample does not appear to have undergone the same extent of the smoothing.

4.3.2 Porosity Changes

With a change in thickness, a corresponding reduction in the pore volume, and therefore the porosity, is expected. The relationship with normalized porosity $\left(\varepsilon/\varepsilon_0\right)$ is explored with respect to the residual strain of each individual sample in **Fig. 4-8**.

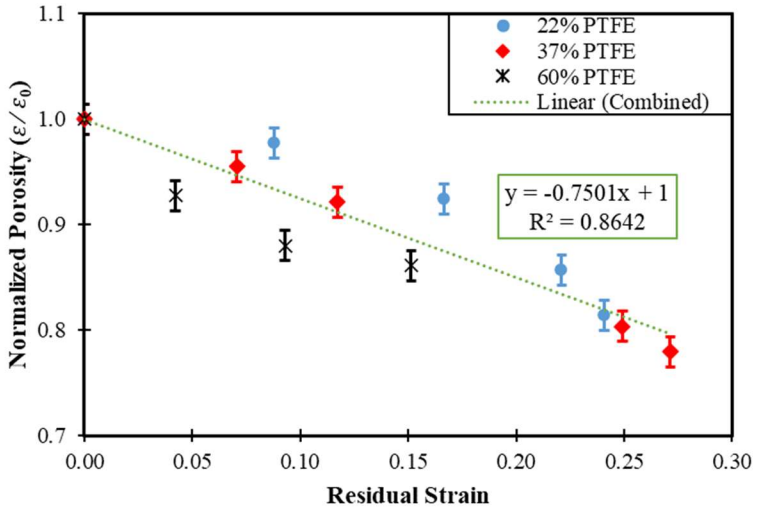

Fig. 4-8. The relationship between the residual strain and normalized porosity of the PTFE-treated Toray TGP-H-120 samples.

4.3.3 Mean Pore Radius Changes

In addition to the reduction in the pore volume, it is expected that the larger pores would preferentially decrease before the smaller pores. This would present itself as a decrease in the mean pore radius with increasing compression. This can be seen in **Fig. 4-9**.

The same mean pore radii data can also be compared to the porosity of the samples, as seen in **Fig. 4-10**. A strong linear relationship between the mean pore radius and the porosity was unexpected. The analytical relationship between the pore radius and the pore volume is typically to the power of 2 or 3, depending on the assumption of cylindrical or spherical pores, respectively. While not shown, the corresponding R^2 for a linear model comparing the mean pore radius squared is equal to 0.784, owing to significant deviations at the smaller mean pore sizes.

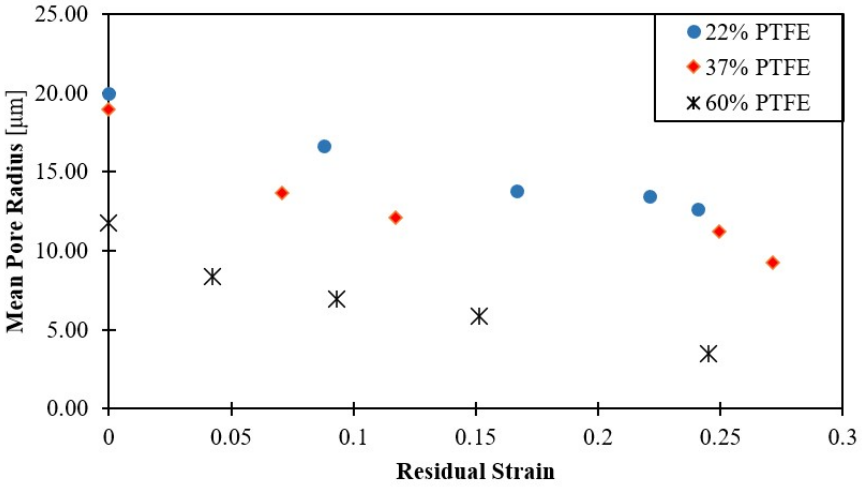

Fig. 4-9. Decreasing mean pore radii with increasing change in thickness of the GDL samples.

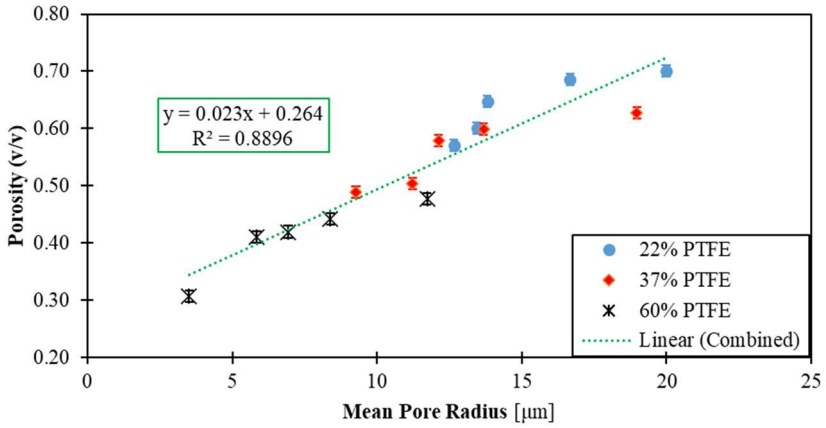

Fig. 4-10. A strong correlation between the mean pore radius and the normalized pore volume (porosity).

4.4 Compression Effects on Diffusion

It must be re-iterated that, at this current time, the sample requirements for the diffusion measurements in the Loschmidt Cell and the Method of Standard Porosimetry do not allow for non-destructive testing. The sample size requirements are smaller for the PSD study and, thus, was completed after all of the compressions and diffusion measurements. The porosity was then back calculated based on the validated assumption that the changes in thickness are a result of changes in porosity. This distinction is noted in the corresponding figure, **Fig. 4-11**,by explicitly referring to "Theoretical Porosity".

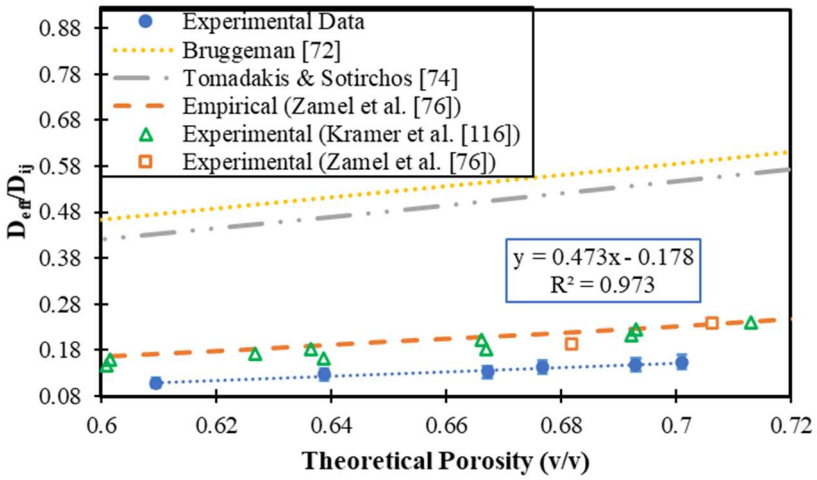

Fig. 4-11. Experimental results of 22% PTFE sample plotted with theoretical porosity against normalized effective diffusion coefficient (to bulk diffusion coefficient). Results compared to experimental data [76, 116] and empirical models [72, 74, 76] from uncompressed GDL samples.

The linearity of the relationship in **Fig. 4-11** highlights two important conclusions: (i) the validation of the primary assumption of the serial testing and (ii) the differences from the non-linear empirical models relating porosity to the diffusivity.

4.4.1 Validation of Serial Testing

The principle assumption for the serial testing of the GDL is that, by using the same sample over a series of compressions, the primary change in variable is porosity. Other material properties, such as PTFE and tortuosity, would effectively be controlled across data points. This distinction is the main difference from the traditional parallel testing employed in all of the previous studies. The compression of the PTFE loaded samples did not alter the mass and, presumably, the presence of PTFE. The assumption of controlled tortuosity will be validated in this section.

Porosity and tortuosity are two of the most important predictive parameters in predicting diffusivity of a given sample. This relationship is typically presented as:

$$\mathcal{D}_{\text{eff}} = \frac{\mathcal{D}_{ij}}{\tau}\varepsilon \tag{4-1}$$

where $\mathcal{D}_{\text{eff}}$ is the effective diffusion coefficient, $\mathcal{D}_{ij}$ is the bulk binary diffusion coefficient, ε is the porosity, and τ is the tortuosity. The effective diffusion coefficient is that which is calculated from the data from the Loschmidt Cell. The bulk binary diffusion

coefficient is a value dependent only on the gas species, temperature, and pressure. The tortuosity of a porous medium is calculated from this relationship.

Since temperature, pressure, and gas species are controlled in the diffusion measurements, the bulk binary diffusion coefficient is a constant. Coupled with the linearity of the effective diffusion coefficient and theoretical porosity, this implies that the tortuosity factor, and tortuosity, is also constant. This observation serves to validate the principle assumption for the serial testing of the GDL.

4.4.2 Differences from Empirical Models of Diffusion

All of the popularized empirical models for predicting diffusivity employ a non-linear relationship with porosity. These empirical models are typically developed from hundreds of data points from various sources. The data was collected using uncompressed GDL samples and simplified GDL structures (in the absence of binder and PTFE) in the numerical models owing to some of the deviations from experimental results. Despite the overall non-linear relationship of these empirical models, particularly within the range of porosities between 0.50 to 0.80, the relationship is seemingly linear as sampled in **Fig. 4-12**.

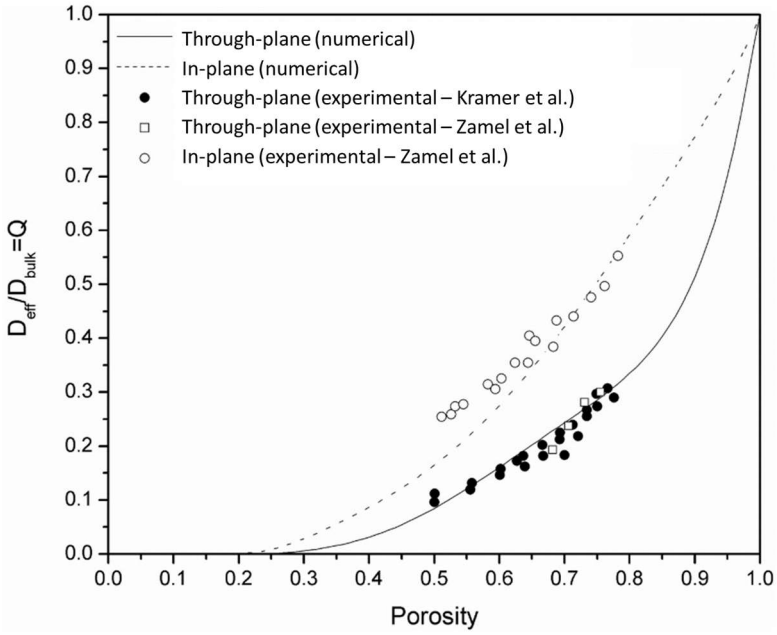

Fig. 4-12. The Zamel *et al.* correlation to previous experimental results. Image was adapted from [76].

Some of the differences in the results between the experimental results and the empirical models, as seen in **Fig. 4-11**, is likely that the parameters controlling porosity in an uncompressed sample, for example manufacturing process, differ from the parameters to changes in porosity as a result of compression. The latter, which was investigated in this research, could be combined with an empirical model to capture the effect of changes in porosity due to strain by the relationship:

$$\frac{\mathcal{D}_{\text{eff}}}{\mathcal{D}_{ij}} = \frac{\mathcal{D}_{\text{eff}}}{\mathcal{D}_{\text{eff},0}} \cdot \frac{\mathcal{D}_{\text{eff},0}}{\mathcal{D}_{ij}} \tag{4-2}$$

Where $\frac{\mathcal{D}_{\text{eff}}}{\mathcal{D}_{\text{eff},0}}$ is the ratio of the effective diffusion coefficients of the strained-to-unstrained, respectively, as obtained from the experimental results, and $\frac{\mathcal{D}_{\text{eff},0}}{\mathcal{D}_{ij}}$ is calculated from an empirical model. Due to the relatively good fit of Zamel's *et al.* correlation compared to Bruggeman and Tomadakis and Sotirchos, this model will be used in the development of the new correlation.

By plotting the normalized change in thickness (residual strain) against the normalized diffusion coefficient of the sample, as seen in **Fig. 4-13**, a strongly linear relationship is observed.

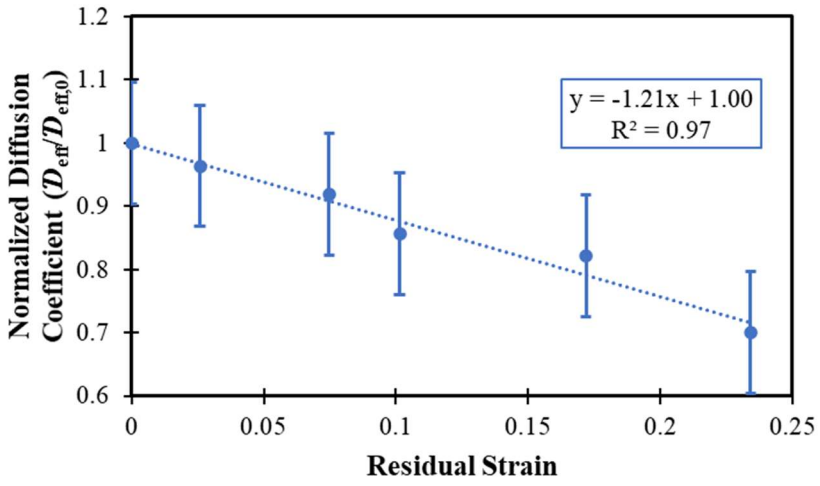

Fig. 4-13. A linear trend relating normalized thickness changes to diffusion coefficients of a 22% PTFE loading sample of TGP-H-120.

This linear relationship can be combined with Zamel's *et al.* correlation to form a new correlation that serves to predict the effective diffusion coefficient due to compressive strain:

$$\frac{\mathcal{D}_{\text{eff}}}{\mathcal{D}_{ij}} = (1 - 1.21\mathit{s}) \cdot \left\{1 - 2.76\varepsilon_0 \cosh(3\varepsilon_0 - 1.92)\left[\frac{3(1-\varepsilon_0)}{3-\varepsilon_0}\right]\right\} \qquad (4\text{-}3)$$

where s is the strain of the GDL sample. This new correlation is plotted with the experimental results in **Fig. 4-14**. Despite its appearances, as evidenced from the exaggerated vertical axis, there is a strong fit (R^2 = 0.970) between the proposed correlation and the results. The rest of the differences is likely arising from Zamel's *et al.* correlation having the tendency to overestimate the value of the normalized effective diffusion coefficient at a porosity of about 0.70, as seen in **Fig. 4-12**, due to simplifications in the GDL structure in the development of that correlation.

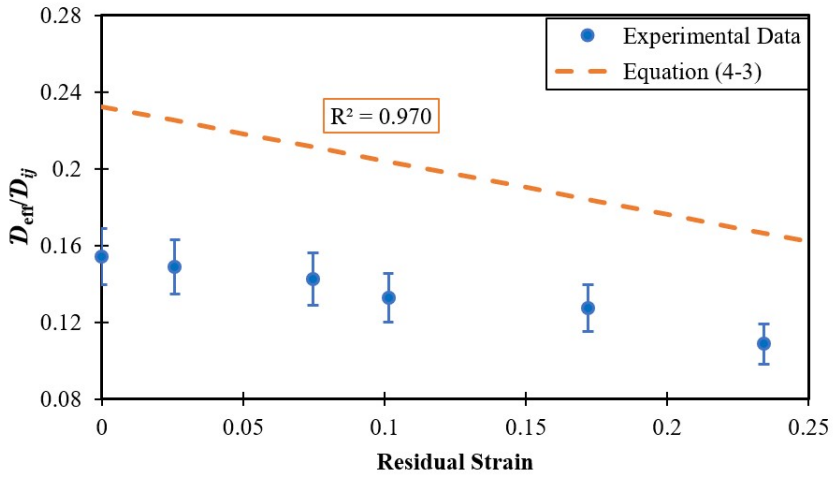

Fig. 4-14. The proposed correlation from **Equation (4-3)** to the experimental results.

With serial testing of GDL samples and a non-destructive means to measure porosity and diffusion, more fine-tuning of the empirical models could be made. PTFE loading and tortuosity can be indirectly controlled in the data set and the strength of each variable can be assessed. After which time, these variables can be incorporated into future models for diffusion through a carbon paper GDL.

4.5 Compression Effects on Permeability

4.5.1 Residual Strain and Permeability

In an attempt to reconcile the dimensional differences for the permeability constant, a comparison of the residual strain was investigated. By comparing the square of the residual strain to the normalized permeability, as seen in **Fig. 4-15**, a dimensionally compatible correlation can potentially be derived.

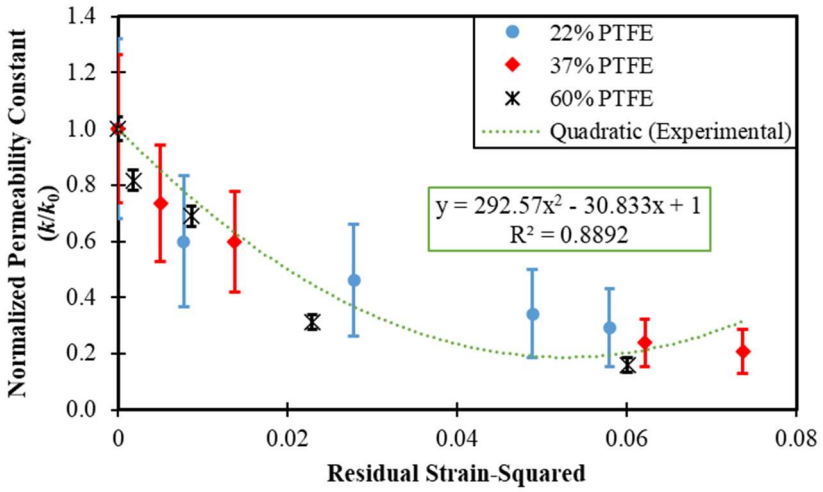

Fig. 4-15. Attempt to correlate the dimensionally-compatible residual strain squared to normalized permeability.

While this quadratic correlation fits quite well, it is poorly supported by any theoretical basis. It is deemed that residual strain is unsuitable to accurately correlate to permeability.

4.5.2 Mean Pore Radius and Permeability

In fluid mechanics, in order to generalize the pressurized flow through an irregular conduit, the flow is often related to a comparable circular conduit. This concept is referred to hydraulic radius, r_{hyd}, and is calculated as [112]:

$$r_{\text{hyd}} = \frac{A}{P} \tag{4-4}$$

where A is the cross-sectional area of the conduit and P is the perimeter. In the calculation of the mean pore radius, it is taken as the integration down the length of the flow path. Functionally, this gives the formulation mean pore radius, $\bar{r}_{\text{pore}}$, as [112]:

$$\bar{r}_{\text{pore}} = \frac{V_{\text{pore}}}{S_{\text{pore}}} \tag{4-5}$$

where V_{pore} is the total pore volume, calculated as the product of the porosity and sample volume, and S_{pore} is the total pore surface area, obtained from the pore size distribution curve. The summary of this correlation can be found in **Fig. 4-16**.

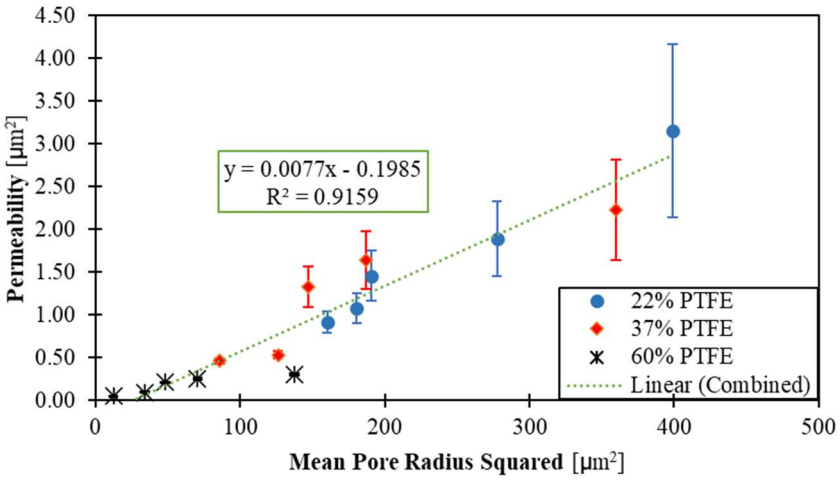

Fig. 4-16. Correlating the mean pore radius squared to the permeability constant. This relationship shows strong linearity.

The strong linearity of the results suggests that the permeability of a carbon paper GDL is strongly correlated to the mean pore radius. The deviations of some of the individual data points is likely arising from the differences of sample-to-sample variations, such as PTFE loading and tortuosity. This result is consistent with knowledge of fluid mechanics and is dimensionally-sound.

4.5.3 The Importance of Masking Small Pore Sizes

The raw pore size distribution reveals a large number of small pores. These small pore sizes significantly increase both the uncertainty of the calculated mean pore size and the total surface area. As shown in **Fig. 4-17**, there is significant scattering of the data in contrast to **Fig. 4-16**. As convective mass flow assumes a continuum, the Knudsen number should be less than 0.1. With the mean flow path of oxygen gas to be 70 nm [69], the corresponding pore radius should be greater than 350 nm. This is even greater than the minimum pore radius, 3.2 nm [54], that can be reasonably measured by MSP. These small pores contribute over 95% of the total pore surface area, heavily skewing the calculated mean pore radius towards the small sizes [31] resulting in a poor linear correlation.

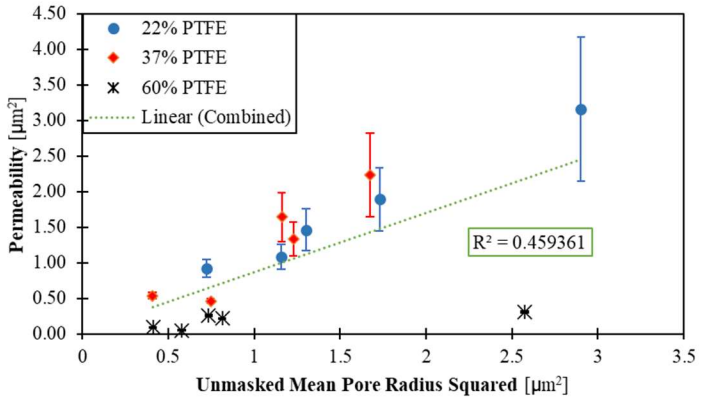

Fig. 4-17. Relating the unmasked mean pore radius (accounting for the full pore size range) squared to the permeability constant shows significant deviation from linearity. The presence of a high number of small non-conducting pores alters the calculation (**Equation (3-6)**) of mean pore radius in an unpredictable manner.

4.5.4 Porosity and Permeability

Traditionally, the results from permeability studies correlate the convective mass transport to the porosity of the sample. Numerous models have been developed from datasets like the one found in **Fig. 4-18**. The differences between the models can arise from the sample-to-sample variations within the datasets as a result of parallel testing. It is evident from **Fig. 4-18** that the 60% PTFE loaded sample data could be used in conjunction with either of the other PTFE loaded samples to derive 2 different models.

Furthermore, the correlations developed in this research, as found in **Fig. 4-10** and **Fig. 4-16**, could be combined to predict the permeability from the porosity. This is also seen to be a strong fit ($R^2 = 0.874$) in **Fig. 4-18**.

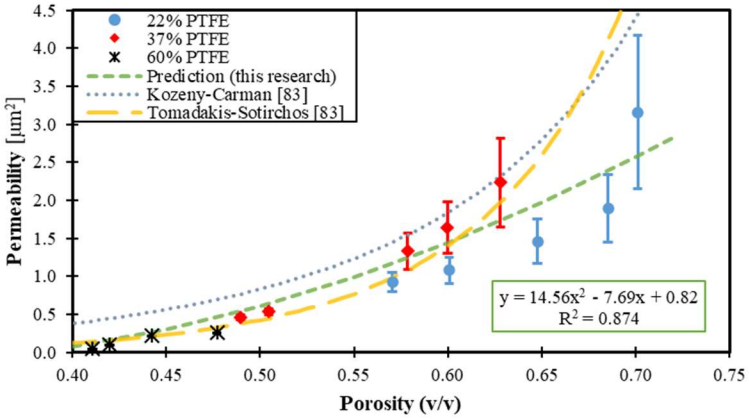

Fig. 4-18. Traditional plot comparing porosity to permeability with experimental data. Results also compared to Kozeny-Carman empirical model with Mean Intercept Length [83] and Tomadakis-Sotirchos empirical random walk model [83]. The average fiber diameter in the TGP-H-120 samples was 8.0 µm.

4.6 Compression Effects on Water Droplet Contact Angles

The static contact angle of de-ionized water on the surfaces of the compressed GDL samples were measured using the sessile drop method with a goniometer. Through the use of image analysis, the software was able to determine the apparent water droplet contact angle. The only available comparable study [18] correlated the compression to the contact angles as shown in **Fig. 4-19**. Aldakheel *et al.* [18] only investigated a single Toray sample, TGP-H-090, with a 5% PTFE loading, among other commercial brands.

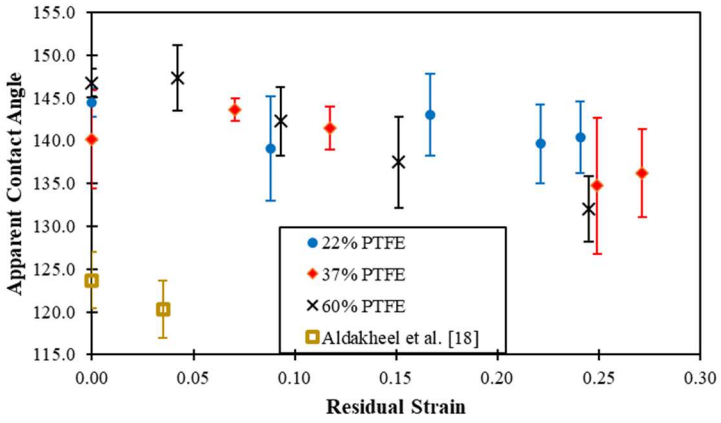

Fig. 4-19. Changes in water droplet static contact angle in response to a series of compressions.

The general observation is that with increased residual strain, there is a decline in the apparent contact angle of the water droplet on the surface of the GDL. With our limited analytical understanding of a water droplet on an inhomogeneous surface, the change in contact angle is a result of the reduced roughness on the surface [18]. However, accounting for the uncertainty in the collected data, this conclusion is not complete. Referring to **Fig. 4-7,** with large amounts of strain, there is a visible change in the geometry of the fibers on the surface. The 22% PTFE sample studied in this thesis research shows almost no change in the contact angle despite significant smoothing of the surface and change in thickness. While the 37% PTFE sample does appear to show a decreasing trend in the contact angle, it is strongly evident with the 60% PTFE sample.

It may be that there is a critical porosity at which the contact angle starts to statistically decrease. The same data is plotted against porosity in **Fig. 4-20**. With relatively large changes to the sample's native porosity, a noticeable drop in the contact angle is observed. The scatter observed in the higher porosity range is due to the differences in PTFE loading, which serve to repel water from the material. Despite the drop in the contact angle, all of the samples remain hydrophobic.

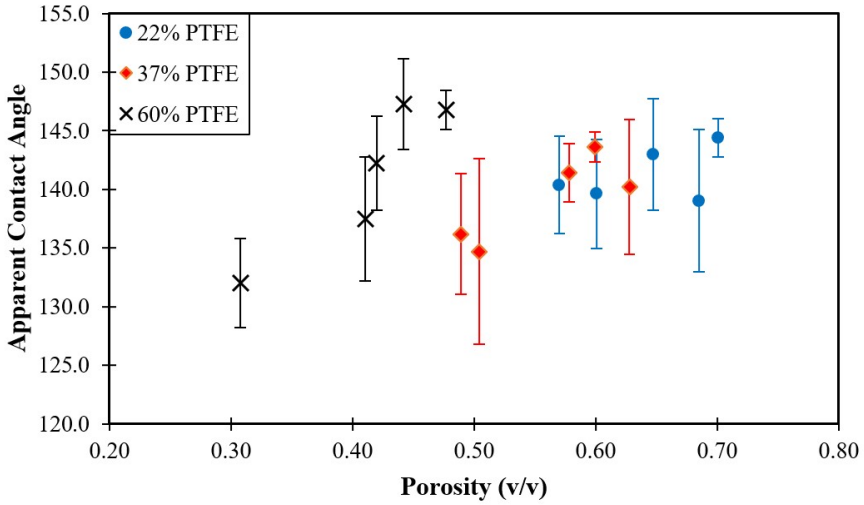

Fig. 4-20. Relating the apparent contact angle to the porosity of the sample.

4.6.1 Comparison to Theoretical Models

To develop a correlation to the observed contact angle accounting for an inhomogeneous surface, the Cassie-Baxter model is explored [42]. In addition, two modifications to the theory are considered: the Wenzel model and an adaptation from García-Salaberri's *et al.* on the relationship between the surface porosity and bulk porosity [55]. Each of these models have similar systems of equations, as summarized in **Table 4-1.**

The Cassie-Baxter model, Equations 1 and 2 in **Table 4-1**, serves to relate the cumulative surface energies interacting with the water droplet to the fraction of each interface. There are three different interactions: water-carbon fiber, water-PTFE, and water-air. The reference contact angles used in this study were 80.2°, 110°, and 180° for carbon fiber, PTFE, and air, respectively [99]. The advantage of this base model is that the surface roughness is integrated into the formulation [27].

These models show their differences in the third equation. For the Cassie-Baxter model, it is assumed that there is a direct correlation of the fractions of water-PTFE and water-carbon fiber interactions to the volume ratio of the two materials. This would be consistent with the observation of the separation of PTFE from the carbon fibers at higher compressions, leading to more carbon fiber exposed [11]. The volume ratio is determined from the PTFE loading (mass/mass) and reference densities of 2.0 $g \cdot cm^{-3}$ and 2.16 $g \cdot cm^{-3}$ for the pure carbon fiber and PTFE, respectively [99]. García-Salaberri et al. developed a correlation of the surface porosity of the TGP-H-120 samples with respect to the bulk porosity of the sample. Their finding was that the surface porosity of the GDL was

always greater than the inner core regions of the sample such that the surface porosity was about 13.2% greater than the bulk porosity [55]. The value of surface porosity is then equated to f_{air}, the ratio of the bottom of the water droplet interacting with the pore spaces. Finally, the Wenzel model assumes that all of the pores are filled with water and, therefore, reduces the system of equations to 2 equations and 2 unknowns.

Table 4-1. System of equations for the Cassie-Baxter model and 2 modified models. Equation 3 is an operating assumption to be able to solve the system.

	Cassie-Baxter	**Adaptation from García-Salaberri**	**Wenzel**
Equation 1	$\cos\theta_{\text{app}} = \sum f_i \cos\theta_i$		
Equation 2	$\sum f_i = 1$		
Equation 3	${f_{\text{PTFE}}}/{f_{\text{CF}}} = {V_{\text{PTFE}}}/{V_{\text{CF}}}$	$f_{\text{air}} \propto \varepsilon_{\text{bulk}}$	$f_{\text{air}} = 0$

Where θ_{app} is the apparent contact angle, as observed, f_i is the fraction of the water droplet interacting with species *i*, θ_i is the reference contact angle for species *i*, and *i* can be either carbon fiber (CF), PTFE, or air.

When attempting to solve these system of equations, it was found that only the Cassie-Baxter model would consistently converge to a solution. The adaptation from García-Salaberri *et al.* revealed some convergence with the 22% PTFE and fewer compressions but failed to converge for all of the 60% PTFE sample data. Additionally, the Wenzel model failed to converge for all observed contact angles for all samples. This is expected since the smallest observed contact angle was 132°, which is greater than the reference contact angle for water-PTFE. In order to solve the equations, f_{air} must be greater than zero.

While earlier attempts failed to correlate the observed contact angle to various material properties, a correlation between f_{air}, or surface porosity, and the contact angle is considered in **Fig. 4-21**. Several conclusions can be made from this relationship. While the bulk porosities for the different PTFE loadings show great disparity, the initial surface porosity is the same. While all of the samples experienced similar maximum residual strains after the last compression, all with the flattening of the surface fibers, the higher the PTFE loading, the greater the change in surface porosity in response to compression.

The PTFE loading has a relatively weak effect on the contact angle, but account for most of the deviations from linearity.

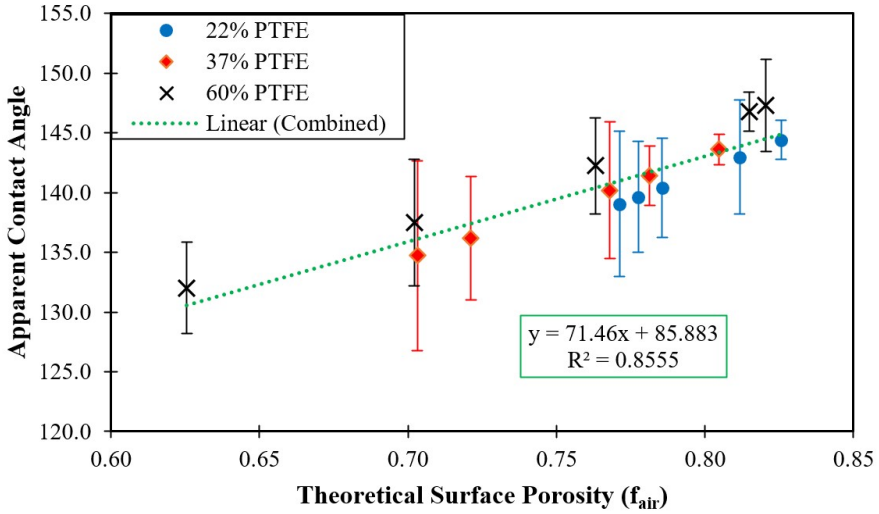

Fig. 4-21. Strong correlation between the surface porosity and apparent contact angle.

With a lower initial porosity of the 60% PTFE sample, and with greater compressions, the core solid region of the sample may be reaching the surface and interacting more with the water droplet. This, in turn, would result in a reduced surface roughness, though the impact of the flattening of the top surface fibers cannot be assessed. Alternatively, the bulk structural properties of the native GDL are not reflected on the surface but, after compression, it does.

Chapter 5

Conclusions and Recommendations

In this research, a comprehensive understanding of the changes in structure to a carbon paper gas diffusion layer (GDL) is thoroughly investigated through experimental techniques. By employing serial testing, a deeper understanding on the effects of pore structure on gas transport and water droplet contact angles is established. The effectiveness of this investigation is a result of a series of non-destructive experimental methods which include: surface visualization by optical microscopy, the Loschmidt Cell for the measurement of the effective diffusion coefficient and the measurement of permeability, the Method of Standard Porosimetry (MSP), and the sessile drop method for contact angle measurements. Due to its accessibility and ease of use, optical microscopy allowed for visually inspecting the same locations on each sample after every compression. The Loschmidt Cell, operating on Fick's second law of diffusion, is used to study the effective diffusion coefficient. Darcy's law is used to investigate the gas permeability of the samples. These characterizations are then coupled with the MSP, which is based on the principle of capillary equilibrium, is used to characterize the microstructure of the GDL with each compression with respect to the porosity, pore size distribution (PSD), pore surface area, and mean pore radius. A goniometer is used to measure the water contact angle on the surface of the GDL samples. All of the instruments used in this thesis research are available in our laboratory. Many assumptions are employed and investigated for their validity.

5.1 Conclusions

In this thesis research, experimental methods are utilized to develop a comprehensive understanding between the changes to the pore structure of a carbon paper GDL to the changes in gas diffusion, gas permeation, and water droplet contact angles. While some assumptions were validated prior to the start of the research, and others validated throughout the studies, all assumptions are found to be sound. The key conclusions from this thesis research are:

- The principle working assumption of the serial testing, whereby the serial compression of the same sample serves to isolate changes to porosity and pore size distribution, is validated by the linear relationship ($R^2 = 0.974$) existing between the normalized effective diffusion coefficient, $\mathcal{D}_{\text{eff}}/\mathcal{D}_{ij}$, and the porosity, ε, such that:

$$\mathcal{D}_{\text{eff}}/\mathcal{D}_{ij} = 0.473\varepsilon - 0.178$$

  Serial compression has the added benefit of reducing the cost of the samples tested by almost an order of magnitude.
- The polytetrafluoroethylene (PTFE) treatment, in addition to aiding in overall water management, enhances the structural integrity of the Toray TGP-H-120 samples. The baseline PTFE condition data were voided because this condition cannot adequately maintain its integrity with serial compression. This serves to highlight the risk involved with serial testing.
- When investigating the mean pore radius of the carbon fiber samples, it is necessary to mask the smaller pores to minimize the uncertainty that these pores contribute towards the calculations. As convective mass transport assumes a continuum, it is best to operate in the Knudsen number < 0.1. This corresponds to a mean pore radius of 350 nm. This masking of the non-conducting pore sizes reveals strong relationships to various transport parameters.
- A strong linear correlation ($R^2 = 0.890$) is found between the mean pore radius ($\bar{r}_{\text{pore}}$) and the normalized pore volume (porosity). Such that:

$$\text{porosity}\ (\varepsilon) = 0.023\bar{r}_{\text{pore}}[\mu\text{m}] + 0.264$$

  This is contrary to expectations where the relationship should be quadratic or cubic owing to the relationship between length and volume, depending on the assumption of pore shapes.

- As changes in porosity and pore structure from compression are governed by different parameters as those set by many empirical models, the normalized effective diffusion coefficient can be strongly correlated (R^2 = 0.970) by a combination of functions of strain ($\mathcal{s}$) and initial porosity (ε_0) such that:

$$\frac{\mathcal{D}_{\text{eff}}}{\mathcal{D}_{ij}} = (1 - 1.21\mathcal{s}) \cdot \left\{1 - 2.76\varepsilon_0 \cosh(3\varepsilon_0 - 1.92)\left[\frac{3(1-\varepsilon_0)}{3-\varepsilon_0}\right]\right\}$$

- The permeability constant, with units length squared, is traditionally correlated to porosity. However, relating the square of the mean pore radius reveals a strong linear relationship (R^2 = 0.916) with permeability. Such that:

$$\text{permeability } (k)\ [\mu\text{m}^2] = 0.008\left(\bar{r}_{\text{pore}}\ [\mu\text{m}]\right)^2 - 0.198$$

  This relationship is dimensionally compatible and agrees with the concept of hydraulic radius in fluid mechanics with respect to convective mass flow. Deviations from linearity are likely attributed to the sample-to-sample variation that inherently exists in the commercially available GDL samples. This correlation can be combined with the proposed porosity correlation to reasonably predict (R^2 = 0.874) the permeability (k) from the porosity (ε).
- The decrease in water droplet contact angle after compression has traditionally been attributed to the flattening of the curvature of the carbon fibers on the surface of the GDL, effectively reducing the surface roughness. Based on comparable visual observations, the underlying GDL material approaches the surface where it begins to interact with the water droplet. This explanation also results in an effective reduction to the surface roughness.
- By assuming that the fractions of water-PTFE and water-carbon fiber are related to the volume ratio as determined by the PTFE loading (mass/mass), the Cassie-Baxter model can robustly be solved to yield the fraction of water-air, or surface porosity. This surface porosity is weakly correlated to the PTFE loading or initial porosity but shows a strong linear relationship (R^2 = 0.856) to the observed contact angle. Such that:

$$\theta_{\text{app}}\ [^\circ] = 71.5 f_{\text{air}} + 85.9$$

  Deviations from the linearity are likely owed to the different PTFE loadings as the middle PTFE loading (37% in this study) trends in between the other two PTFE loadings.

5.2 Recommendations

To address the limitations of the mass commercialization of PEM fuel cell technology, further optimizations are required. The correlations presented in this research can be used to further improve numerical studies into the optimization of fuel cell design, especially as it pertains at higher current densities where reactant mass transport is the source of most of the energy losses in fuel cells. The recommendations for this research are summarized as follows:

- A non-destructive method to measure the diffusion coefficient and the pore structure is required to be developed to provide a more comprehensive understanding with appropriate parameters.
- A more comprehensive empirical model should be developed to relate all of the relevant parameters for mass transport through porous media, such as mean pore radius, PTFE content, and tortuosity. It would be interesting to investigate if such a model can be expanded to account for different commercially available GDL samples.
- Finally, if these comprehensive models are developed, to incorporate them into numerical simulations. It would be interesting to investigate the simulation's response to dynamic operating conditions. Differences with *in-situ* fuel cell testing could reveal further deficiencies in other aspects of fuel cell operations.

REFERENCES

[1] R. Rath, P. Kumar, S. Mohanty, and S. K. Nayak, “Recent advances, unsolved deficiencies, and future perspectives of hydrogen fuel cells in transportation and portable sectors,” *Int. J. Energy Res.*, vol. 43, no. 15, pp. 8931–8955, Dec. 2019, doi: 10.1002/er.4795.

[2] T. Hua, R. Ahluwalia, L. Eudy, G. Singer, B. Jermer, N. Asselin-Miller, S. Wessel, T. Patterson, and J. Marcinkoski, “Status of hydrogen fuel cell electric buses worldwide,” *J. Power Sources*, vol. 269, pp. 975–993, 2014, doi: 10.1016/j.jpowsour.2014.06.055.

[3] X. Li, *Principles of Fuel Cells*. New York: Taylor & Francis, 2006.

[4] J. Zhao and X. Li, “A review of polymer electrolyte membrane fuel cell durability for vehicular applications: Degradation modes and experimental techniques,” *Energy Conversion and Management*, vol. 199. Elsevier Ltd, 01-Nov-2019, doi: 10.1016/j.enconman.2019.112022.

[5] J. Zhao, “Catalyst Layers in Polymer Electrolyte Membrane Fuel Cells: Formation, Characterization and Performance,” *Ph.D. Diss. MME, Univ. Waterloo*, 2019.

[6] S. Tsushima and S. Hirai, “In situ diagnostics for water transport in proton exchange membrane fuel cells,” *Progress in Energy and Combustion Science*, vol. 37, no. 2. Pergamon, pp. 204–220, 01-Apr-2011, doi: 10.1016/j.pecs.2010.06.001.

[7] J. Wang, J. Yuan, and B. Sundén, “On electric resistance effects of non-homogeneous GDL deformation in a PEM fuel cell,” *Int. J. Hydrogen Energy*, vol. 42, no. 47, pp. 28537–28548, 2017, doi: 10.1016/j.ijhydene.2017.09.119.

[8] J. Wang, J. Yuan, and B. Sundén, “Modeling of inhomogeneous compression effects of porous GDL on transport phenomena and performance in PEM fuel cells,” *Int. J. Energy Res.*, vol. 41, no. 7, pp. 985–1003, 2017, doi: 10.1002/er.3687.

[9] J. Millichamp, T. J. Mason, T. P. Neville, N. Rajalakshmi, R. Jervis, P. R. Shearing, and D. J. L. Brett, “Mechanisms and effects of mechanical compression and dimensional change in polymer electrolyte fuel cells - A review,” *J. Power Sources*, vol. 284, pp. 305–320, 2015, doi: 10.1016/j.jpowsour.2015.02.111.

[10] N. K. Shrivastava, A. Chatterjee, and T. A. L. Harris, “Effect of cell compression on the performance of a non–hot-pressed MEA for PEMFC,” *Int. J. Energy Res.*, vol. 44, no. 1, pp. 370–387, Jan. 2020, doi: 10.1002/er.4933.

[11] J. Park, H. Oh, T. Ha, Y. Il Lee, and K. Min, “A review of the gas diffusion layer in proton exchange membrane fuel cells: Durability and degradation,” *Appl. Energy*, vol. 155, pp. 866–880, Oct. 2015, doi: 10.1016/j.apenergy.2015.06.068.

[12] D. K. Qiu, L. F. Peng, P. Y. Yi, X. M. Lai, H. Janßen, and W. Lehnert, “Multiscale numerical model for contact resistance prediction in the proton exchange membrane fuel cell,” *ECS Trans.*, vol. 80, no. 8, pp. 73–85, 2017, doi: 10.1149/08008.0073ecst.

[13] V. Senthil Velan, G. Velayutham, N. Rajalakshmi, and K. S. Dhathathreyan, “Influence of compressive stress on the pore structure of carbon cloth based gas diffusion layer investigated by capillary flow porometry,” *Int. J. Hydrogen Energy*, vol. 39, no. 4, pp. 1752–1759, Jan. 2014, doi: 10.1016/j.ijhydene.2013.11.038.

[14] Xiaohui Yan, Chen Lin, Zhifeng Zheng, Junren Chen, Guanghua Wei, and Junliang Zhang, “Effect of clamping pressure on liquid-cooled PEMFC stack performance considering inhomogeneous gas diffusion layer compression,” *Appl. Energy*, p. 114073, 2019, doi: 10.1016/j.apenergy.2019.114073.

[15] A. M. Dafalla and F. Jiang, “Stresses and their impacts on proton exchange membrane fuel cells: A review,” *Int. J. Hydrogen Energy*, vol. 43, no. 4, pp. 2327–2348, 2018, doi: 10.1016/j.ijhydene.2017.12.033.

[16] N. Ge, P. Shrestha, M. Balakrishnan, D. Ouellette, A. K. C. Wong, H. Liu, C. H. Lee, J. K. Lee, and A. Bazylak, “Resolving the gas diffusion layer substrate land and channel region contributions to the oxygen transport resistance of a partially-saturated substrate,” *Electrochim. Acta*, vol. 328, Dec. 2019, doi: 10.1016/j.electacta.2019.135001.

[17] M. Ashrafi and M. Shams, “Effects of heterogeneous surface of gas diffusion layers on droplet transport in microchannels of PEM fuel cells,” 2016, doi: 10.1016/j.ijhydene.2015.11.096.

[18] F. Aldakheel, M. S. Ismail, K. J. Hughes, D. B. Ingham, L. Ma, M. Pourkashanian, D. Cumming, and R. Smith, “Gas permeability, wettability and morphology of gas diffusion layers before and after performing a realistic ex-situ

compression test," *Renew. Energy*, 2019, doi: 10.1016/j.renene.2019.11.109.

[19] N. Zamel and X. Li, "Effective transport properties for polymer electrolyte membrane fuel cells - With a focus on the gas diffusion layer," *Prog. Energy Combust. Sci.*, vol. 39, no. 1, pp. 111–146, 2013, doi: 10.1016/j.pecs.2012.07.002.

[20] J. T. Gostick, M. W. Fowler, M. D. Pritzker, and M. A. Ioannidis, "Porosimetry and Characterization of the Capillary Properties of Gas Diffusion Media," CRC Press, 2012, pp. 514–531.

[21] S. Didari, T. A. L. Harris, W. Huang, S. M. Tessier, and Y. Wang, "Feasibility of periodic surface models to develop gas diffusion layers: A gas permeability study," *Int. J. Hydrogen Energy*, vol. 37, no. 19, pp. 14427–14438, 2012, doi: 10.1016/j.ijhydene.2012.06.100.

[22] J. M. Morgan and R. Datta, "Understanding the gas diffusion layer in proton exchange membrane fuel cells. I. How its structural characteristics affect diffusion and performance," *J. Power Sources*, vol. 251, pp. 269–278, 2014, doi: 10.1016/j.jpowsour.2013.09.090.

[23] V. Norouzifard and M. Bahrami, "Deformation of PEM fuel cell gas diffusion layers under compressive loading: An analytical approach," *J. Power Sources*, vol. 264, pp. 92–99, 2014, doi: 10.1016/j.jpowsour.2014.04.057.

[24] X.-Z. Yuan, H. Li, E. Gu, W. Qian, F. Girard, Q. Wang, T. Biggs, and M. Jaeggle, "Measurements of GDL Properties for Quality Control in Fuel Cell Mass Production Line," *World Electr. Veh. J.*, vol. 8, no. 2, pp. 422–430, Jun. 2016, doi: 10.3390/wevj8020422.

[25] E. H. Majlan, D. Rohendi, W. R. W. Daud, T. Husaini, and M. A. Haque, "Electrode for proton exchange membrane fuel cells: A review," 2018, doi: 10.1016/j.rser.2018.03.007.

[26] C. Lim and C. Y. Wang, "Effects of hydrophobic polymer content in GDL on power performance of a PEM fuel cell," *Electrochim. Acta*, vol. 49, pp. 4149–4156, 2004, doi: 10.1016/j.electacta.2004.04.009.

[27] Y. Si and Z. Guo, "Nanoscale Superhydrophobic nanocoatings: from materials to fabrications and to applications," vol. 7, p. 5922, 2015, doi: 10.1039/c4nr07554d.

[28] V. Manzi-Orezzoli, A. Mularczyk, P. Trtik, J. Halter, J. Eller, T. J. Schmidt, and P. Boillat, "Coating Distribution Analysis on Gas Diffusion Layers for Polymer Electrolyte Fuel Cells by Neutron and X-ray High-Resolution Tomography," *ACS*

Omega, vol. 4, no. 17, pp. 17236–17243, Oct. 2019, doi: 10.1021/acsomega.9b01763.

[29] C. Chan, N. Zamel, X. Li, and J. Shen, "Experimental measurement of effective diffusion coefficient of gas diffusion layer/microporous layer in PEM fuel cells," *Electrochim. Acta*, vol. 65, pp. 13–21, 2012, doi: 10.1016/j.electacta.2011.12.110.

[30] C. F. Berg, "Permeability Description by Characteristic Length, Tortuosity, Constriction and Porosity," *Transp Porous Med*, vol. 103, pp. 381–400, 2014, doi: 10.1007/s11242-014-0307-6.

[31] J. Zhao, S. Shahgaldi, A. Ozden, I. E. Alaefour, X. Li, and F. Hamdullahpur, "Geometric pore surface area and fractal dimension of catalyzed electrodes in polymer electrolyte membrane fuel cells," *Int. J. Energy Res.*, pp. 1–9, Oct. 2018, doi: 10.1002/er.4260.

[32] J. Crank, *The Mathematics of Diffusion*, 2nd ed. Oxford University Press, 1975.

[33] J. Geertsma, "Estimating the Coefficient of Inertial Resistance in Fluid Flow Through Porous Media," *Soc. Pet. Eng. J.*, vol. 14, no. 05, pp. 445–450, 1974, doi: 10.2118/4706-PA.

[34] S. Park, J. W. Lee, and B. N. Popov, "A review of gas diffusion layer in PEM fuel cells: Materials and designs," *International Journal of Hydrogen Energy*, vol. 37, no. 7. Elsevier Ltd, pp. 5850–5865, 01-Apr-2012, doi: 10.1016/j.ijhydene.2011.12.148.

[35] H. Li, Y. Tang, Z. Wang, Z. Shi, S. Wu, D. Song, J. Zhang, K. Fatih, J. Zhang, H. Wang, Z. Liu, R. Abouatallah, and A. Mazza, "A review of water flooding issues in the proton exchange membrane fuel cell," *Journal of Power Sources*, vol. 178, no. 1. Elsevier, pp. 103–117, 15-Mar-2008, doi: 10.1016/j.jpowsour.2007.12.068.

[36] P. Gopalan and S. G. Kandlikar, "Effect of Channel Material on Water Droplet Dynamics in a PEMFC Gas Channel," *J. Electrochem. Soc.*, vol. 160, no. 6, pp. F487–F495, 2013, doi: 10.1149/2.030306jes.

[37] D. H. Ye, E. Gauthier, M. J. Cheah, J. Benziger, and M. Pan, "The effect of gas diffusion layer compression on gas bypass and water slug motion in parallel gas flow channels," *AIChE J.*, vol. 61, no. 1, pp. 355–367, Jan. 2015, doi: 10.1002/aic.14686.

[38] A. Bazylak, J. Heinrich, N. Djilali, and D. Sinton, "Liquid water transport between graphite paper and a solid surface," *J. Power Sources*, vol. 185, pp.

1147–1153, 2008, doi: 10.1016/j.jpowsour.2008.07.031.

[39] K. Jiao and X. Li, “Effect of surface dynamic wettability in proton exchange membrane fuel cells,” *Int. J. Hydrogen Energy*, vol. 35, pp. 9095–9103, 2010, doi: 10.1016/j.ijhydene.2010.05.027.

[40] S. B. Park and Y. il Park, “Fabrication of gas diffusion layer (GDL) containing microporous layer using flourinated ethylene prophylene (FEP) for proton exchange membrane fuel cell (PEMFC),” *Int. J. Precis. Eng. Manuf.*, vol. 13, no. 7, pp. 1145–1151, 2012, doi: 10.1007/s12541-012-0152-x.

[41] rame-hart instrument Co., “rame-hart Contact Angle,” 2020. [Online]. Available: http://ramehart.com/contactangle.htm.

[42] A. B. D. Cassie and S. Baxter, “WETTABILITY OF POROUS SURFACES,” 1944.

[43] I. Taymaz and M. Benli, “Numerical study of assembly pressure effect on the performance of proton exchange membrane fuel cell,” *Energy*, vol. 35, no. 5, pp. 2134–2140, 2010, doi: 10.1016/j.energy.2010.01.032.

[44] X. Zhou, Z. Niu, Y. Li, X. Sun, Q. Du, J. Xuan, and K. Jiao, “Investigation of two-phase flow in the compressed gas diffusion layer microstructures,” *Int. J. Hydrogen Energy*, vol. 44, no. 48, pp. 26498–26516, Oct. 2019, doi: 10.1016/j.ijhydene.2019.08.108.

[45] P. A. Gigos, Y. Faydi, and Y. Meyer, “Mechanical characterization and analytical modeling of gas diffusion layers under cyclic compression,” *Int. J. Hydrogen Energy*, vol. 40, no. 17, pp. 5958–5965, 2015, doi: 10.1016/j.ijhydene.2015.02.136.

[46] T. J. Mason, J. Millichamp, T. P. Neville, A. El-Kharouf, B. G. Pollet, and D. J. L. Brett, “Effect of clamping pressure on ohmic resistance and compression of gas diffusion layers for polymer electrolyte fuel cells,” *J. Power Sources*, vol. 219, pp. 52–59, 2012, doi: 10.1016/j.jpowsour.2012.07.021.

[47] P. K. Sow, S. Prass, P. Kalisvaart, and W. Mérida, “Deconvolution of electrical contact and bulk resistance of gas diffusion layers for fuel cell applications,” *Int. J. Hydrogen Energy*, vol. 40, no. 6, pp. 2850–2861, 2015, doi: 10.1016/j.ijhydene.2014.12.110.

[48] T. Lee and C. Yang, “A parametric study on the deformation of gas diffusion layer in PEM fuel cell,” *J. Mech. Sci. Technol.*, vol. 34, 2020, doi:

10.1007/s12206-019-1227-8.

[49] C. H. Chien, Y. L. Hu, T. H. Su, H. T. Liu, C. T. Wang, P. F. Yang, and Y. X. Lu, "Effects of bolt pre-loading variations on performance of GDL in a bolted PEMFC by 3-D FEM analysis," *Energy*, vol. 113, pp. 1174–1187, 2016, doi: 10.1016/j.energy.2016.07.075.

[50] A. Bates, S. Mukherjee, S. Hwang, S. C. Lee, O. Kwon, G. H. Choi, and S. Park, "Simulation and experimental analysis of the clamping pressure distribution in a PEM fuel cell stack," *Int. J. Hydrogen Energy*, vol. 38, no. 15, pp. 6481–6493, 2013, doi: 10.1016/j.ijhydene.2013.03.049.

[51] C. Y. Wen, H. T. Chang, and T. W. Luo, "Simulation methodology on analyzing clamping mode for single proton exchange membrane fuel cell," *J. Mech.*, vol. 27, no. 4, pp. 545–558, 2011, doi: 10.1017/jmech.2011.57.

[52] I. Gatto, F. Urbani, G. Giacoppo, O. Barbera, and E. Passalacqua, "Influence of the bolt torque on PEFC performance with different gasket materials," *Int. J. Hydrogen Energy*, vol. 36, no. 20, pp. 13043–13050, 2011, doi: 10.1016/j.ijhydene.2011.07.066.

[53] S. Yu, J. Hao, J. Li, and L. Zhang, "Effect of distribution of polytetrafluoroethylene on durability of gas diffusion backing in proton exchange membrane fuel cell," *Mater. Res. Bull.*, Feb. 2019, doi: 10.1016/j.materresbull.2019.110684.

[54] J. Zhao, S. Shahgaldi, A. Ozden, I. E. Alaefour, X. Li, and F. Hamdullahpur, "Geometric pore surface area and fractal dimension of catalyzed electrodes in polymer electrolyte membrane fuel cells," *Int. J. Energy Res.*, vol. 43, pp. 3011–3019, Jun. 2019, doi: 10.1002/er.4260.

[55] P. A. García-Salaberri, I. V Zenyuk, A. D. Shum, G. Hwang, M. Vera, A. Z. Weber, and J. T. Gostick, "Analysis of representative elementary volume and through-plane regional characteristics of carbon-fiber papers: diffusivity, permeability and electrical/thermal conductivity," 2018, doi: 10.1016/j.ijheatmasstransfer.2018.07.030.

[56] I. V. Zenyuk, D. Y. Parkinson, L. G. Connolly, and A. Z. Weber, "Gas-diffusion-layer structural properties under compression via X-ray tomography," *J. Power Sources*, vol. 328, pp. 364–376, 2016, doi: 10.1016/j.jpowsour.2016.08.020.

[57] G. Karapetsas, N. T. Chamakos, and A. G. Papathanasiou -, "Related content

Application of a hybrid kinetic-continuum solver to the near wall modelling O Rovenskaya and G Croce-Efficient modelling of droplet dynamics on complex surfaces," *J. Phys. Conf. Ser. OPEN ACCESS*, vol. 547, p. 12028, 2014, doi: 10.1088/1742-6596/547/1/012028.

[58] J. P. James, H. W. Choi, and J. G. Pharoah, "X-ray computed tomography reconstruction and analysis of polymer electrolyte membrane fuel cell porous transport layers," *Int. J. Hydrogen Energy*, vol. 37, no. 23, pp. 18216–18230, 2012, doi: 10.1016/j.ijhydene.2012.08.077.

[59] J. Liu, P. A. García-Salaberri, and I. V. Zenyuk, "Bridging scales to model reactive diffusive transport in porous media," *J. Electrochem. Soc.*, vol. 167, no. 1, 2020, doi: 10.1149/2.0242001JES.

[60] J. T. Gostick, M. W. Fowler, M. A. Ioannidis, M. D. Pritzker, Y. M. Volfkovich, and A. Sakars, "Capillary pressure and hydrophilic porosity in gas diffusion layers for polymer electrolyte fuel cells," *J. Power Sources*, vol. 156, pp. 375–387, 2006, doi: 10.1016/j.jpowsour.2005.05.086.

[61] Z. Yu, R. N. Carter, and J. Zhang, "Measurements of pore size distribution, porosity, effective oxygen diffusivity, and tortuosity of PEM fuel cell electrodes," *Fuel Cells*, vol. 12, no. 4, pp. 557–565, 2012, doi: 10.1002/fuce.201200017.

[62] V. Radhakrishnan and P. Haridoss, "Effect of cyclic compression on structure and properties of a Gas Diffusion Layer used in PEM fuel cells," *Int. J. Hydrogen Energy*, vol. 35, no. 20, pp. 11107–11118, Oct. 2010, doi: 10.1016/j.ijhydene.2010.07.009.

[63] E. C. Kumbur, K. V Sharp, and M. M. Mench, "Validated Leverett Approach for Multiphase Flow in PEFC Diffusion Media II. Compression Effect," *J. Electrochem. Soc.*, vol. 154, no. 12, pp. B1305–B1314, 2007, doi: 10.1149/1.2784285.

[64] P. Mangal, L. M. Pant, N. Carrigy, M. Dumontier, V. Zingan, S. Mitra, and M. Secanell, "Experimental study of mass transport in PEMFCs: Through plane permeability and molecular diffusivity in GDLs," *Electrochim. Acta*, vol. 167, pp. 160–171, 2015, doi: 10.1016/j.electacta.2015.03.100.

[65] J. Yuan and B. Sundén, "On mechanisms and models of multi-component gas diffusion in porous structures of fuel cell electrodes," *Int. J. Heat Mass Transf.*, vol. 69, pp. 358–374, Feb. 2014, doi:

10.1016/J.IJHEATMASSTRANSFER.2013.10.032.

[66] S. Sambandum and V. Ramani, “In Situ Measurement of Oxygen Permeability in Polymer Electrolyte Membranes,” *ECS Trans.*, vol. 25, no. 1, pp. 433–441, 2009.

[67] S. Li, J. Yuan, G. Xie, and B. Sundén, “Effects of agglomerate model parameters on transport characterization and performance of PEM fuel cells,” *Int. J. Hydrogen Energy*, vol. 43, no. 17, pp. 8451–8463, 2018, doi: 10.1016/j.ijhydene.2018.03.106.

[68] J. Shen, J. Zhou, N. G. C. Astrath, T. Navessin, Z. S. Liu, C. Lei, J. H. Rohling, D. Bessarabov, S. Knights, and S. Ye, “Measurement of effective gas diffusion coefficients of catalyst layers of PEM fuel cells with a Loschmidt diffusion cell,” *J. Power Sources*, vol. 196, no. 2, pp. 674–678, 2011, doi: 10.1016/j.jpowsour.2010.07.086.

[69] J. Zhao, S. Shahgaldi, I. Alaefour, S. Yang, and X. Li, “Pore structure and effective diffusion coefficient of catalyzed electrodes in polymer electrolyte membrane fuel cells,” *Int. J. Hydrogen Energy*, vol. 43, no. 7, pp. 3776–3785, 2018, doi: 10.1016/j.ijhydene.2018.01.019.

[70] S. Salari, J. Stumper, and M. Bahrami, “Direct measurement and modeling relative gas diffusivity of PEMFC catalyst layers: The effect of ionomer to carbon ratio, operating temperature, porosity, and pore size distribution,” *Int. J. Hydrogen Energy*, vol. 43, no. 34, pp. 16704–16718, Aug. 2018, doi: 10.1016/j.ijhydene.2018.07.035.

[71] T. R. Marrero and E. A. Mason, “Gaseous Diffusion Coefficients,” *J. Phys. Chem. Ref. Data*, vol. 1, no. 1, pp. 3–118, Jan. 1972, doi: 10.1063/1.3253094.

[72] M. Mitani, “Geometric factor for diffusion in porous media.,” *J. Chem. Eng. Japan*, vol. 17, no. 4, pp. 441–443, Aug. 1984, doi: 10.1252/jcej.17.441.

[73] G. H. Neale and W. K. Nader, “Prediction of transport processes within porous media: Creeping flow relative to a fixed swarm of spherical particles,” *AIChE J.*, vol. 20, no. 3, pp. 530–538, May 1974, doi: 10.1002/aic.690200314.

[74] M. M. Tomadakis and S. V. Sotirchos, “Ordinary and transition regime diffusion in random fiber structures,” *AIChE J.*, vol. 39, no. 3, pp. 397–412, Mar. 1993, doi: 10.1002/aic.690390304.

[75] M. M. Mezedur, M. Kaviany, and W. Moore, “Effect of Pore Structure, Randomness and Size on Effective Mass Diffusivity.”

[76] N. Zamel, X. Li, and J. Shen, “Correlation for the Effective Gas Diffusion Coefficient in Carbon Paper Diffusion Media,” doi: 10.1021/ef900653x.

[77] T. V. Reshetenko, J. St-Pierre, and R. Rocheleau, “Effects of local gas diffusion layer gas permeability variations on spatial proton exchange membrane fuel cells performance,” *J. Power Sources*, vol. 241, pp. 597–607, 2013, doi: 10.1016/j.jpowsour.2013.04.131.

[78] I. S. Hussaini and C. Y. Wang, “Measurement of relative permeability of fuel cell diffusion media,” *J. Power Sources*, vol. 195, no. 12, pp. 3830–3840, 2010, doi: 10.1016/j.jpowsour.2009.12.105.

[79] J. T. Gostick, M. W. Fowler, M. D. Pritzker, M. A. Ioannidis, and L. M. Behra, “In-plane and through-plane gas permeability of carbon fiber electrode backing layers,” *J. Power Sources*, vol. 162, no. 1, pp. 228–238, 2006, doi: 10.1016/j.jpowsour.2006.06.096.

[80] A. Tamayol, F. McGregor, and M. Bahrami, “Single phase through-plane permeability of carbon paper gas diffusion layers,” *J. Power Sources*, vol. 204, pp. 94–99, 2012, doi: 10.1016/j.jpowsour.2011.11.084.

[81] J. Zhao, S. Shahgaldi, I. Alaefour, Q. Xu, and X. Li, “Gas permeability of catalyzed electrodes in polymer electrolyte membrane fuel cells,” *Appl. Energy*, vol. 209, no. October 2017, pp. 203–210, 2018, doi: 10.1016/j.apenergy.2017.10.087.

[82] L. J. Klinkenberg, “The Permeability Of Porous Media To Liquids And Gases,” Jan. 1941.

[83] M. M. Tomadakis and T. J. Robertson, “Viscous permeability of random fiber structures: Comparison of electrical and diffusional estimates with experimental and analytical results,” *J. Compos. Mater.*, vol. 39, no. 2, pp. 163–188, 2005, doi: 10.1177/0021998305046438.

[84] Y. Chen, C. Shen, P. Lu, and Y. Huang, “Role of pore structure on liquid flow behaviors in porous media characterized by fractal geometry,” *Chem. Eng. Process. Process Intensif.*, vol. 87, pp. 75–80, Jan. 2015, doi: 10.1016/j.cep.2014.11.014.

[85] D. Tehlar, R. Flückiger, A. Wokaun, and F. N. Büchi, “Investigation of Channel-to-Channel Cross Convection in Serpentine Flow Fields,” *Fuel Cells*, vol. 10, no. 6, pp. 1040–1049, 2010, doi: 10.1002/fuce.201000034.

[86] K. Jiao, J. Park, and X. Li, “Experimental investigations on liquid water removal from the gas diffusion layer by reactant flow in a PEM fuel cell,” *Appl. Energy*, vol. 87, no. 9, pp. 2770–2777, 2010, doi: 10.1016/j.apenergy.2009.04.041.

[87] R. B. Ferreira, D. S. Falcão, V. B. Oliveira, and A. M. F. R. Pinto, “1D + 3D two-phase flow numerical model of a proton exchange membrane fuel cell,” *Appl. Energy*, vol. 203, pp. 474–495, 2017, doi: 10.1016/j.apenergy.2017.06.048.

[88] Y. Wu, J. I. S. Cho, X. Lu, L. Rasha, T. P. Neville, J. Millichamp, R. Ziesche, N. Kardjilov, H. Markötter, P. Shearing, and D. J. L. Brett, “Effect of compression on the water management of polymer electrolyte fuel cells: An in-operando neutron radiography study,” *J. Power Sources*, vol. 412, pp. 597–605, Feb. 2019, doi: 10.1016/j.jpowsour.2018.11.048.

[89] U. U. Ince, H. Markötter, M. G. George, H. Liu, N. Ge, J. Lee, S. S. Alrwashdeh, R. Zeis, M. Messerschmidt, J. Scholta, A. Bazylak, and I. Manke, “Effects of compression on water distribution in gas diffusion layer materials of PEMFC in a point injection device by means of synchrotron X-ray imaging,” *Int. J. Hydrogen Energy*, vol. 43, no. 1, pp. 391–406, Jan. 2018, doi: 10.1016/j.ijhydene.2017.11.047.

[90] D. L. Wood, C. Rulison, and R. L. Borup, “Surface Properties of PEMFC Gas Diffusion Layers,” *J. Electrochem. Soc.*, vol. 157, pp. 195–206, 2010, doi: 10.1149/1.3261850.

[91] V. Parry, G. Berthomé, and J.-C. Joud, “Wetting properties of gas diffusion layers: Application of the Cassie-Baxter and Wenzel equations,” *Appl. Surf. Sci.*, vol. 258, pp. 5619–5627, 2012, doi: 10.1016/j.apsusc.2012.02.038.

[92] H. Deng, K. Jiao, Y. Hou, J. W. Park, and Q. Du, “A lattice Boltzmann model for multi-component two-phase gas-liquid flow with realistic fluid properties,” *Int. J. Heat Mass Transf.*, vol. 128, pp. 536–549, 2019, doi: 10.1016/j.ijheatmasstransfer.2018.09.019.

[93] M. Jiang, B. Zhou, and X. Wang, “Comparisons and validations of contact angle models,” *Int. J. Hydrogen Energy*, vol. 43, no. 12, pp. 6364–6378, Mar. 2018, doi: 10.1016/j.ijhydene.2018.02.016.

[94] A. Arvay, E. Yli-Rantala, C. H. Liu, X. H. Peng, P. Koski, L. Cindrella, P. Kauranen, P. M. Wilde, and A. M. Kannan, “Characterization techniques for gas diffusion layers for proton exchange membrane fuel cells - A review,” *Journal of*

Power Sources, vol. 213. pp. 317–337, 01-Sep-2012, doi: 10.1016/j.jpowsour.2012.04.026.

[95] M. Andersson, A. Mularczyk, A. Lamibrac, S. B. Beale, J. Eller, W. Lehnert, and F. N. Büchi, "Modeling and synchrotron imaging of droplet detachment in gas channels of polymer electrolyte fuel cells," *J. Power Sources*, vol. 404, pp. 159–171, Nov. 2018, doi: 10.1016/j.jpowsour.2018.10.021.

[96] E. Planes, G. De Moor, C. Bas, and L. Flandin, "Sliding Angle Characterization of Physicochemical and Roughness Changes of GDL Surfaces after Fuel Cell Operation," *Fuel Cells*, vol. 18, no. 2, pp. 148–159, Apr. 2018, doi: 10.1002/fuce.201700014.

[97] J. T. Sellman and A. D. Santamaria, "Ex-situ probing of PEFC liquid droplet dynamics in the presence of vibration," 2017, doi: 10.1016/j.ijhydene.2017.02.140.

[98] X. Zhang and Y. Qin, "Contact angle hysteresis of a water droplet on a hydrophobic fuel cell surface," *J. Colloid Interface Sci.*, vol. 545, pp. 231–241, Jun. 2019, doi: 10.1016/j.jcis.2019.03.026.

[99] D. L. Wood, C. Rulison, and R. L. Borup, "Surface Properties of PEMFC Gas Diffusion Layers," *J. Electrochem. Soc.*, vol. 157, pp. 195–206, 2010, doi: 10.1149/1.3261850.

[100] D. Froning, J. Brinkmann, U. Reimer, V. Schmidt, W. Lehnert, and D. Stolten, "3D analysis, modeling and simulation of transport processes in compressed fibrous microstructures, using the Lattice Boltzmann method," *Electrochim. Acta*, vol. 110, pp. 325–334, 2013, doi: 10.1016/j.electacta.2013.04.071.

[101] H. Ito, K. Abe, M. Ishida, A. Nakano, T. Maeda, T. Munakata, H. Nakajima, and T. Kitahara, "Effect of through-plane distribution of polytetrafluoroethylene in carbon paper on in-plane gas permeability," *J. Power Sources*, vol. 248, pp. 822–830, 2014, doi: 10.1016/j.jpowsour.2013.10.009.

[102] J. Z. Fishman, H. Leung, and A. Bazylak, "Droplet pinning by PEM fuel cell GDL surfaces," *Int. J. Hydrogen Energy*, vol. 35, no. 17, pp. 9144–9150, Sep. 2010, doi: 10.1016/j.ijhydene.2010.06.027.

[103] S. Didari, A. Asadi, Y. Wang, and T. A. L. Harris, "Modeling of composite fibrous porous diffusion media," *Int. J. Hydrogen Energy*, vol. 39, no. 17, pp. 9375–9386, 2014, doi: 10.1016/j.ijhydene.2014.04.011.

[104] A. Nabovati, J. Hinebaugh, A. Bazylak, and C. H. Amon, “Effect of porosity heterogeneity on the permeability and tortuosity of gas diffusion layers in polymer electrolyte membrane fuel cells,” *J. Power Sources*, vol. 248, pp. 83–90, 2014, doi: 10.1016/j.jpowsour.2013.09.061.

[105] R. R. Rashapov, J. Unno, and J. T. Gostick, “Characterization of PEMFC Gas Diffusion Layer Porosity,” *J. Electrochem. Soc.*, vol. 162, no. 6, pp. 603–612, 2015, doi: 10.1149/2.0921506jes.

[106] M. Piller, D. Casagrande, G. Schena, and M. Santini, “Pore-scale simulation of laminar flow through porous media,” *J. Phys. Conf. Ser.*, vol. 501, no. 1, 2014, doi: 10.1088/1742-6596/501/1/012010.

[107] A. El-Kharouf and R. Steinberger-Wilckens, “The Effect of Clamping Pressure on Gas Diffusion Layer Performance in Polymer Electrolyte Fuel Cells,” *Fuel Cells*, vol. 15, no. 6, pp. 802–812, 2015, doi: 10.1002/fuce.201500088.

[108] D. Bograchev, M. Gueguen, J. C. Grandidier, and S. Martemianov, “Stress and plastic deformation of MEA in fuel cells. Stresses generated during cell assembly,” *J. Power Sources*, vol. 180, no. 1, pp. 393–401, 2008, doi: 10.1016/j.jpowsour.2008.02.048.

[109] M. R. Inc., “MPM&P Research Inc.,” 2017. [Online]. Available: https://mpmandp.com/.

[110] Y. M. Volfkovich, A. V. Sakars, and A. A. Volinsky, “Application of the standard porosimetry method for nanomaterials,” *Int. J. Nanotechnol.*, vol. 2, no. 3, pp. 292–302, 2005, doi: 10.1504/IJNT.2005.008066.

[111] Y. M. Volfkovich and V. S. Bagotzky, “The method of standard porosimetry. 1. Principles and possibilities,” *J. Power Sources*, vol. 48, no. 3, pp. 327–338, Mar. 1994, doi: 10.1016/0378-7753(94)80029-4.

[112] P. C. Carman, “Diffusion and Flow of Gases and Vapours through Micropores. I. Slip Flow and Molecular,” 1950.

[113] Y. Wang and S. Wang, “Evaluation and modeling of PEM fuel cells with the Bruggeman correlation under various tortuosity factors,” *Int. J. Heat Mass Transf.*, vol. 105, pp. 18–23, 2017, doi: 10.1016/j.ijheatmasstransfer.2016.09.030.

[114] N. Khajeh-Hosseini-Dalasm, T. Sasabe, T. Tokumasu, and U. Pasaogullari, “Effects of polytetrafluoroethylene treatment and compression on gas diffusion layer microstructure using high-resolution X-ray computed tomography,” *J.*

Power Sources, vol. 266, pp. 213–221, 2014, doi: 10.1016/j.jpowsour.2014.05.004.

[115] C. J. Tseng and S. K. Lo, "Effects of microstructure characteristics of gas diffusion layer and microporous layer on the performance of PEMFC," *Energy Convers. Manag.*, vol. 51, no. 4, pp. 677–684, 2010, doi: 10.1016/j.enconman.2009.11.011.

[116] D. Kramer, S. A. Freunberger, R. Flü ckiger, I. A. Schneider, A. Wokaun, F. N. Bü chi, and G. G. nther Scherer, "Electrochemical diffusimetry of fuel cell gas diffusion layers," 2007, doi: 10.1016/j.jelechem.2007.09.014.